

Identifiers

DOI 10.46298/jtcam.10172

HAL hal-03817644v3

History

Received Oct 18, 2022

Accepted Apr 18, 2023

Published Aug 18, 2023

Associate Editor

Anna PANDOLFI

Reviewer

Anonymous

Open Review

OAI hal-04114094

Supplementary Material

Data

DOI 10.5281/zenodo.8256346

Licence

CC BY 4.0

©The Authors

Crack branching at low tip speeds: spilling the T Elie EID^{1,2}, Rian SEGHIR¹, and Julien RÉTHORÉ¹¹ Nantes Université, École Centrale Nantes, CNRS, GeM, UMR 6183, Nantes, F-44000, France² LaMCoS, Laboratoire de Mécanique des Contacts et des Structures, UMR 5259-CNRS, Lyon, France

Using the criterion that a crack will extend along the direction of maximum circumferential stress, this paper demonstrates the influence of the coupling between the crack-parallel T -stress and the tip speed v_c on the directional (in)stability of dynamics cracks in brittle materials, i.e., branching, turning and limiting velocities. The proposed (in)stability criterion evolves within the theory of dynamic fracture with the introduction of a reference distance r_c ahead of the crack-tip to incorporate the contribution of the higher-order terms in the asymptotic solution of the elastic crack-tip fields. The theoretical aspect is first explored, a methodology to numerically (and experimentally) advocate the instability—as a co-action of T -stress and a fast running crack—is then proposed and validated on a classical branching benchmark. An experimental setup combining Ultra-High-Speed High-Resolution imaging with advanced Digital Image Correlation algorithms and a novel crack-branching inertial impact test enables for never-seen-before quantification of the rich dynamical behaviour of the fracture. This permits the experimental validation of the developed crack (in)stability criterion.

Keywords: dynamic fracture, T -stress, crack branching, limiting crack velocity

1 Crack (in)stabilities within the theory of dynamic fracture

Dynamic fracture mechanics predicts that the Rayleigh wave speed c_R is the limiting velocity of a mode I stable crack propagation. However, experimental observations show the existence of limiting velocities typically around 40 % of c_R , above which, instabilities emerge and eventual branching occurs. The limiting velocities are found to depend on the material, the geometry and boundary conditions. Besides, numerical simulations such as phase-field approaches to dynamic fracture are shown to successfully reproduce experimental crack patterns, i.e., initiation, coalescence, branching positions and branching angles (Liu et al. 2016; Pham et al. 2017; Ren et al. 2019; Ambati et al. 2015). In the same spirit, it is found that the tip speed of stable cracks in phase-field simulations of dynamic fracture are also limited around the same order of magnitudes ($\sim 40\%$ of c_R) as the experiments, with some discrepancy, e.g., in (Borden et al. 2012).

The instantaneous crack (in)stabilities, i.e., branching/turning and limiting velocities under mode I are at the core of this paper; more specifically, the ability to explain crack branching at slower tip speeds than the ones predicted within the theory of dynamic fracture mechanics is sought. It is noted that the (in)stability in question does by no mean regard the instability as considered by Lyapunov; it is more about the directional stability (Streit and Finnie 1980; Ramulu and Kobayashi 1983).

In the literature, a multitude of criteria were proposed for crack extension and fracture (Cotterell and Rice 1980; Erdogan and Sih 1963; Hussain et al. 1974; Palaniswamy and Knauss 1978; Williams and Ewing 1972). The most fundamental ones assume that the crack should advance in the direction that maximises the energy release rate (Hussain et al. 1974; Palaniswamy and Knauss 1978) (energy-based criteria). An alternative theory suggests that locally, the crack will choose the direction at which the local stress field at the tip is symmetric (similar to mode I, no mode II sliding) to advance (stress-based criteria). Among these criteria, the maximum circumferential stress criterion ($\sigma_{\theta\theta}$) was first proposed in quasi-statics by Erdogan and Sih

(1963). It was adopted in dynamics by many authors (Williams and Ewing 1972; Streit and Finnie 1980; Finnie and Saith 1973). Its success rests on its simplicity since an analysis of the stress state near the crack-tip is sufficient to predict its extension behaviour:

$$\theta_0 = \arg \max_{\theta} \sigma_{\theta\theta}, \quad \text{with } \sigma_{\theta\theta} > 0 \quad (1)$$

where θ_0 is the direction that maximizes $\sigma_{\theta\theta} > 0$.

The maximum circumferential stress criterion has previously been analysed in the vicinity of a moving crack-tip (v_c) by considering the leading terms, i.e., the stress intensity factors SIF (Freund 1998). By proposing an expression of the stress fields around a moving crack-tip (v_c) as a function of (SIF) terms, the stresses at position (r, θ) from the crack tip are given by Freund (1998) as:

$$\sigma_{ij}(r, \theta, v_c) = \sum_{k=I,II} \frac{K_{kD}}{\sqrt{2\pi r}} S_{ij}^k(\theta, v_c) \quad (2)$$

For mode I opening:

$$\begin{aligned} S_{11}^I(\theta, v_c) &= \frac{1}{D(v_c)} \left[(1 + \beta_s^2)(1 + 2\beta_d^2 - \beta_s^2) \frac{\cos(\theta_d/2)}{\sqrt{\gamma_d}} - 4\beta_s\beta_d \frac{\cos(\theta_s/2)}{\sqrt{\gamma_s}} \right] \\ S_{12}^I(\theta, v_c) &= \frac{2\beta_d(1 + \beta_s^2)}{D(v_c)} \left[\frac{\sin(\theta_d/2)}{\sqrt{\gamma_d}} - \frac{\sin(\theta_s/2)}{\sqrt{\gamma_s}} \right] \\ S_{22}^I(\theta, v_c) &= -\frac{1}{D(v_c)} \left[(1 + \beta_s^2)^2 \frac{\cos \theta_d/2}{\sqrt{\gamma_d}} - 4\beta_s\beta_d \frac{\cos(\theta_s/2)}{\sqrt{\gamma_s}} \right] \end{aligned} \quad (3)$$

and for mode II plane shear loading:

$$\begin{aligned} S_{11}^{II}(\theta, v_c) &= -\frac{2\beta_s}{D(v_c)} \left[(1 + 2\beta_d^2 - \beta_s^2) \frac{\sin(\theta_d/2)}{\sqrt{\gamma_d}} - (1 + \beta_s^2) \frac{\sin(\theta_s/2)}{\sqrt{\gamma_s}} \right] \\ S_{12}^{II}(\theta, v_c) &= \frac{1}{D(v_c)} \left[4\beta_s\beta_d \frac{\cos \theta_d/2}{\sqrt{\gamma_d}} - (1 + \beta_s^2) \frac{\cos(\theta_s/2)}{\sqrt{\gamma_s}} \right] \\ S_{22}^{II}(\theta, v_c) &= \frac{2\beta_s(1 + \beta_d^2)}{D(v_c)} \left[\frac{\sin(\theta_d/2)}{\sqrt{\gamma_d}} - \frac{\sin(\theta_s/2)}{\sqrt{\gamma_s}} \right] \end{aligned} \quad (4)$$

with $D(v_c) = 4\beta_s\beta_d - (1 + \beta_s^2)^2$, $\beta_d = \sqrt{1 - (v_c/c_d)^2}$, $\tan \theta_d = \beta_d \tan \theta$, $\beta_s = \sqrt{1 - (v_c/c_s)^2}$, $\tan \theta_s = \beta_s \tan \theta$ and $\gamma_d = \sqrt{1 - (v_c \sin \theta/c_d)^2}$ and $\gamma_s = \sqrt{1 - (v_c \sin \theta/c_s)^2}$ where c_d , c_s and c_R are dilatational, shear and Rayleigh wave speeds respectively. Figure 1(a) shows the typical angular variation of a normalised circumferential tensile stress around the moving crack-tip for a material of Poisson ratio $\nu = 0.3$ for several values of normalised crack speeds v_c . Figure 1(b) shows the direction of maximum circumferential stress $\sigma_{\theta\theta}$ that is computed following Equation (1).

Consequently, it is seen that the circumferential stress reaches a maximum $\sigma_{\theta\theta}^0$ at a $\theta_0 \neq 0$ angle when the crack-tip speed exceeds a critical velocity threshold $\simeq 0.72c_R$. This feature was first observed by Yoffe (1951) 60 years ago. Although this derivation was able to predict that the limiting velocity for a stable crack is lower than c_R ($\simeq 0.72c_R$), unfortunately, it could not explain the lower critical velocities observed in experiments and equivalently in phase-field simulations ($\simeq 0.4 - 0.5c_R$).

On the theory of brittle fracture and its foundation

LEFM and its dynamic counterpart are found around the notion of small-scale yielding. The small scale yielding incorporates the notion that the leading SIF terms still govern the deformation state inside a small confined zone (fracture process zone) at the crack-tip. However, it is becoming more recognised that non-singular stresses can become significant depending on the geometry and loading of the specimen, and the role of T -stress for instance has been extensively studied in quasi-static (Gupta et al. 2015) and also in fatigue to determine the influence of T -stress on the size of the plastic zone at the crack tip (Brugier et al. 2015; Brugier 2017).

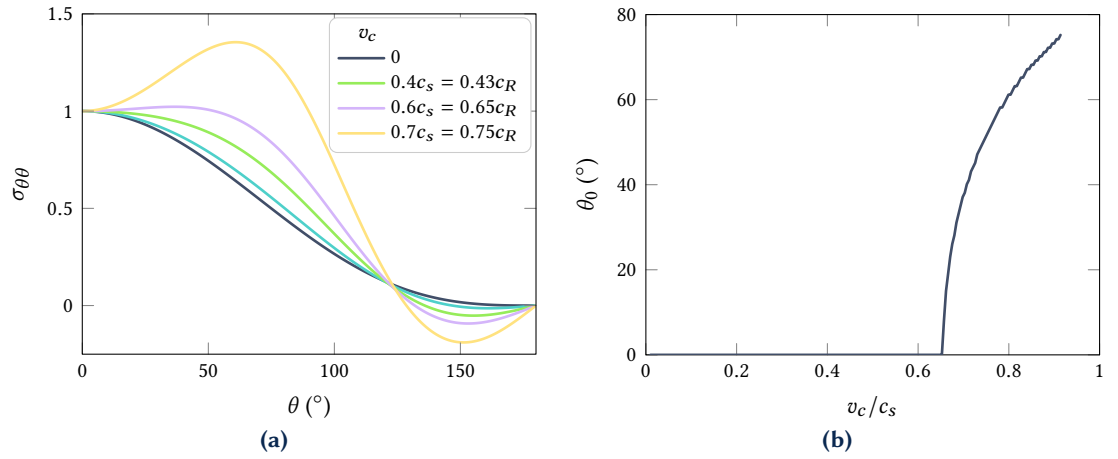


Figure 1 (a) Angular distribution of $\sigma_{\theta\theta}$ for various v_c (Yoffe 1951); (b) Direction θ_0 maximising $\sigma_{\theta\theta}$ as a function of the normalised crack-tip speed.

In dynamic fracture, we believe that the finite size of the medium in real life applications and in the simulations of fracture brings reflections of stress-waves from the boundaries to interact with the running cracks and modifies the stress state near the crack tip. This might be the reason the limiting speeds observed experimentally or numerically are much smaller than the theoretical predictions. A quantification of these modifications is needed.

2 Incorporation of T -stress

The analysis of the angular stress distribution as a criterion for crack (in)stability is retained, however, we build on the work of Ramulu and Kobayashi (1983) and introduce higher-order terms in the analysis. As per (Ramulu and Kobayashi 1983), a non-singular uniform term, i.e., T -stress could be added to the expression of the stresses parallel to the crack path. For a semi-infinite crack propagating along the 1 direction at crack-tip speed v_c under mixed loading, the stress component σ_{11} becomes

$$\sigma_{11}(r, \theta, v_c) = \sum_{k=I,II} \frac{K_{kD}}{\sqrt{2\pi r}} S_{11}^k(\theta, v_c) + T. \quad (5)$$

When incorporating T -stress in the analytical solution, it is assumed that fracture growth is dictated by the stress field at a given distance r_c ahead of the crack-tip introducing thus a non-local effect through this length scale r_c at which the contribution of the higher-order terms become significant to the fracture process. Beyond enabling the assessment of higher-order terms, the assumption of such given distance was shown to be physically reasonable by many authors (Rice and Johnson 1970; Ritchie et al. 1973; Streit and Finnie 1980) arguing that r_c corresponds to a distance from a crack-tip at which micro-defects can coalesce as an extension of the crack. Of course, this r_c would depend on the materials' heterogeneities at the microscopic levels.

When adding T -stress to the stress solution, Equation (1) should be rewritten at a distance r from the crack-tip as:

$$\theta_0(r, v_c, T) = \arg \max_{\theta} \sigma_{\theta\theta}(r, \theta, v_c, T, K_{ID}) \quad (6)$$

with $\sigma_{\theta\theta} > 0$. Within this context, Ramulu and Kobayashi (1983) proposed a criterion that predicts the instabilities for crack-tip speeds $v_c < 0.67c_s = 0.72c_R^1$ based on the introduction of a reference distance scale r_o . From Equation (6), finding the expression of θ_0 , and setting it to zero (stable), a sufficient condition for stability emerges as a function of K_{ID} , T -stress, and the

¹ In this range of crack-tip speeds $0 \leq v_c \leq 0.67c_s = 0.72c_R$, the classical solution (without non-singular terms) would give stable crack propagation ($\theta_0 = 0$).

crack velocity v_c . Indeed, the crack propagation is considered stable when it tends to propagate along its direction of growth, i.e., at $\theta_0 = 0$, and unstable else-wise. This condition brings forth a unique reference distance $r = r_o$ as a function of the K_{ID} , T -stress and the crack velocity v_c , valid in $0 \leq v_c \leq 0.67c_s = 0.72c_R$. r_o represents a distance below which the crack propagation is dominated by the SIF, i.e., the direction of propagation is along the extension of the crack in the range $0 \leq v_c \leq 0.67c_s = 0.72c_R$, which means that the directional stability of a mode I propagating crack is maintained. For a material of critical distance r_c , the sufficient stability condition relating r_c to the (in)stability reference distance r_o reads $r_o \geq r_c$. So r_c falls in an SIF-dominated region (stable crack propagation).

Figure 2 shows a schematic representation of the criterion. Stable and unstable cases are shown. The red zone corresponds to a zone where K is not dominant, and far-field stresses play a major role in determining the angular distribution of the crack direction. The blue zone corresponds to the stability zone, in which SIF (K_{ID}) is dominant.

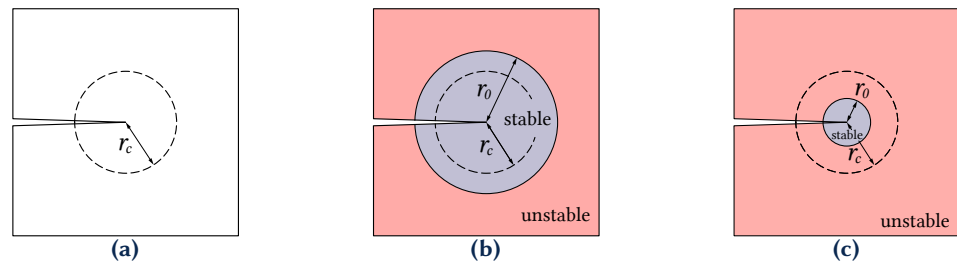


Figure 2 Stability criterion $r_o \geq r_c$ as proposed by Ramulu and Kobayashi (1983): r_c is a material parameter stating the distance at which damage may occur while r_o can be seen as a representation of the stress field. In $r \leq r_o$, a K -dominant zone is omnipresent. The criterion stands for $0 \leq v_c \leq 0.67c_s = 0.72c_R$.

For an arbitrary material of critical crack growth distance r_c , Figure 3 shows the evolution of r_o at fixed T -stress as a function of the crack-tip speeds. It also shows the influence of T -stress on

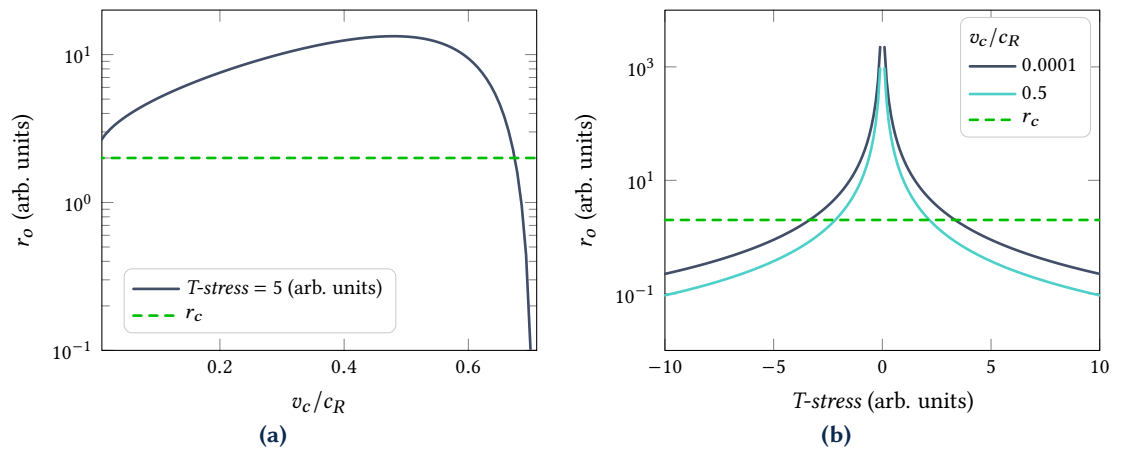


Figure 3 Stability criterion $r_o \geq r_c$. (a) Influence of the crack-tip speeds; (b) T -stress. At T -stress = 0, the criterion gives an ever-stable crack in the range $0 \leq 0.67c_s = 0.72c_R$, in line with the classical solution (Yoffe 1951).

r_o at two fixed speeds, one comparable to a quasi-static propagation and another one at $v_c = 0.5c_R$. As per Figure 3(a), this translates to an unstable crack growth for a crack starting $v_c \approx 0.67c_R$ —for the considered arbitrary material, under an arbitrary T -stress. Of course, T -stress = 0 would yield an ever-stable crack under this criterion, within its range of application $0 \leq 0.67c_s = 0.72c_R$, coherently with the classical solution (Yoffe 1951).

In Figure 3(b), Ramulu and Kobayashi (1983)’s criterion predicts unstable crack propagation even under negative T -stress at low crack-tip speeds, which is in contradiction with multiple works (see e.g., in Gupta et al. (2015) for a review of the influence of T -stress on crack propagation). Moreover, it is evident how a faster running crack (e.g., $v_c = 0.5c_R$ versus $v_c = 0.0001c_R$) is more prone to instabilities at lower T -stress levels. Further, this criterion might suffer from some limitations:

- The inability to incorporate branching at fast running cracks from the classical solution, for example, under complex stress-wave propagation and reflection (in real-life applications/advanced simulations), T -stress would be extremely volatile and building a criterion that is able to predict instabilities in the absence and presence of T -stress is crucial;
- Prediction of crack instability at negative T -stress under near quasi-static loading, which was contradicted by various authors (Gupta et al. 2015).

Remark 1 In (Ramulu and Kobayashi 1983; Ramulu and Kobayashi 1985; Kobayashi and Ramulu 1985), experimental validation of the proposed criterion is followed and the determination of the critical distance r_c is made across multiple experiments by determining r_o^{inst} , which is the value of r_o just before the instability, and noting $r_c = r_o^{inst}$. In the 1980's, the ability to estimate highly resolved (in time) SIF, T -stress and crack-tip speeds experimentally was lacking, and r_c was considered as the smallest r_o computed across the experiments.

3 Material (in)stability map: a comprehensive criterion

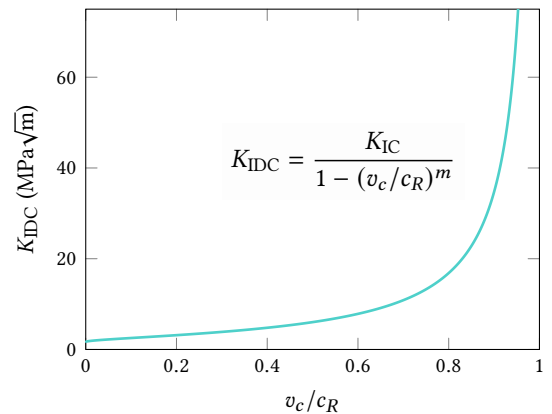
We build on (Ramulu and Kobayashi 1983) to further shed light on the role played by the T -stress on the angular distribution of the stresses and hence on the dynamic (in)stabilities. We expose the assumptions required for building an illustrative example showcasing the (in)stability criterion:

1. Fracture is driven by the stress-field in the local neighbourhood of a moving crack-tip (Freund 1998).
2. The material obeys the maximum circumferential stress criterion.
3. Dynamically, the crack advances at $K_{ID} = K_{IDC}$, and its propagation behaviour law is known (e.g., following Kanninen and Popelar (1985)'s crack propagation law relating K_{IDC} to K_{IC} and the crack tip speed v_c).
4. A reference distance r_c that adequately combines the effect of the T -stress and K_{ID} along with the crack-tip speed v_c is known and is a material parameter.

To build a map that embodies a criterion for the transition between stable and unstable crack propagation for crack-tip speeds $0 \leq v_c \leq c_R$, the goal is to determine, for a given material (knowing its density ρ , its elastic properties E , ν , its fracture toughness K_{IDC} —or crack propagation behaviour— $K_{IDC} \propto v_c$, K_{IC} , etc., and its material constant r_c) the loadings (in terms of fracture mechanics, i.e., K_{ID} , T -stress, v_c) under which crack growth is stable and the loadings under which crack growth is not stable.

For this purpose, a large range of T -stress and crack-tip speeds v_c are swept (representing the crack propagation behaviour) and the analytical solution is evaluated to find the direction θ_0 of maximum circumferential stress $\sigma_{\theta\theta}^0$ at distance r_c from the crack-tip, see Equation (6). This allows the construction of a 2D surface that gives θ_0 as a function of crack-tip speed v_c and T -stress.

Figure 4 Empirical law (Kanninen and Popelar 1985) with $K_{IC} = 1.66 \text{ MPa}\sqrt{\text{m}}$ and $m = 0.465$.



We take an arbitrary set of material parameters, see Table 1, and assume that as the crack advances at $K_{IDC} = K_{ID}$, the material obeys the empirical law

$$K_{IDC} = \frac{K_{IC}}{1 - (v_c/c_R)^m} \tag{7}$$

proposed by Kanninen and Popelar (1985) and relating the critical dynamic stress intensity factor K_{IDC} to its static counterpart K_{IC} where K_{IC} is the static counterpart of the fracture toughness and m is a material constant.

The material (in)stability map is constructed and showcased in Figure 5(a) in the $(v_c, T\text{-stress})$ -space. We analyse $T\text{-stress}$ between -30 MPa and $+30$ MPa. Figure 5(b) shows the equivalence in the $(K_{IDC}, T\text{-stress})$ -space, since K_{IDC} can be related to v_c via Equation (7).

ρ	E	ν	K_{IC}	m	r_c	c_d	c_s	c_R
1200 kg/m ³	6 GPa	0.3	1.66 MPa√m	0.465	2 mm	2594 m/s	1387 m/s	1287 m/s

Table 1 Arbitrary material for the illustrative example showcasing the material (in)stability map.

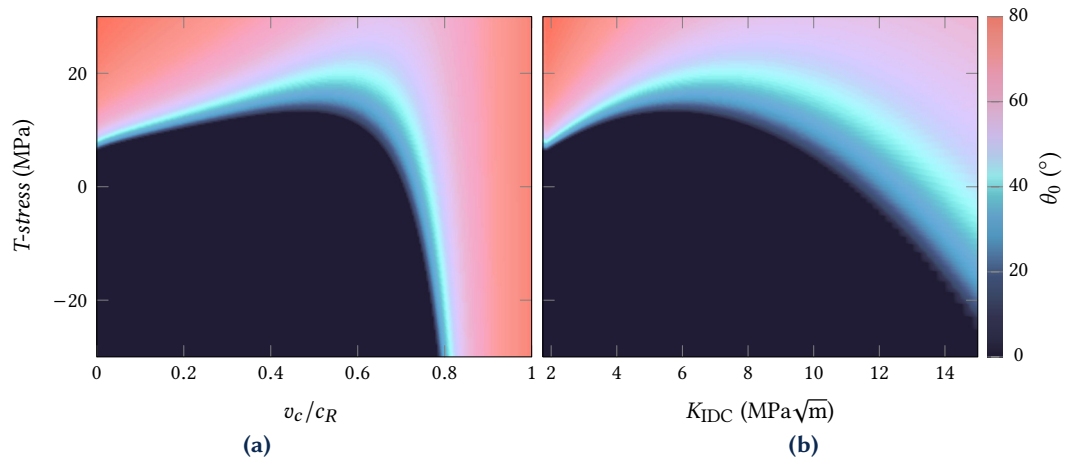


Figure 5 (In)stability map showing the emergence of both stable and unstable crack propagation.

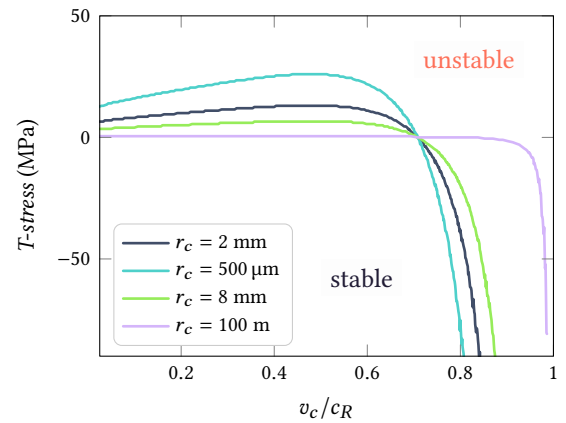
In this range of $T\text{-stress}$ shown in Figure 5, one can observe the following:

- At $T\text{-stress} = 0$, the classical solution is recovered, see Figure 1(b).
- For crack-tip speeds $0 \leq v_c \leq 0.8c_R$, a negative $T\text{-stress}$ stabilises the crack.
- Even at slow crack-tip speeds, e.g., $v_c = 0.05c_R$, the presence of a $T\text{-stress}$ can foster instabilities and eventual branching.
- Above $v_c = 0.8c_R$, independently of the values of $T\text{-stress}$, instability is prominent.
- Dependently of the intensity of $T\text{-stress}$, different limiting velocities can be reached (transition zone between stable and unstable crack propagation).
- The sharpness of the transition zone between the stable and unstable crack growth varies with the crack-tip speed and $T\text{-stress}$.

Remark 2 These observations only stand for the (in)stability map herein considered, of course each material would have a unique (in)stability map, e.g., a material with the same mechanical properties but which critical distance r_c is much bigger than 2 mm would withstand even less $T\text{-stress}$ at stable propagation, since more weight would be given to the contribution of the uniform $T\text{-stress}$ on the stress-state thus modifying its angular distribution away from $\theta_0 = 0$. To show this influence, three equivalent materials are considered and only the reference distance r_c is different for each material $r_c = 2$ mm, 500 μ m, 8 mm (this difference might come for instance from the difference in the distribution of microstructural defects or other in the materials). Figure 6 shows the transition zone between a stable and unstable for the three materials.

Remark 3 A commonly used scheme to ensure directional stability at high crack-tip speeds is to side groove the test pieces. This would normally allow the cracks to reach near-sonic crack-tip speeds. Regarding the fact that the (in)stability map Figure 6 shows a limiting velocity always smaller than c_R , in the case of a side-groove, complex state of stress on the specimen that cannot be taken into account in the (in)stability map are created. So this side grooving exercise is out of the scope of this study.

Figure 6 Influence of r_c on the transition zone in the (in)stability. A synthetic $r_c = 100$ m is added to validate the limiting theoretical velocity at $v_c = c_R$.



Remark 4 We recall that in this directional (in)stability study, the interest is only drawn onto mode I propagating cracks. Once a crack branches, the coexistence of two crack-tips redistributes the stresses. The study thus can no longer be followed.

Remark 5 A mixed-mode loading would affect the direction of propagation of the crack, however, this does not fall in the scope of analysing the (in)stability as seen in this paper (occurring namely at fast-running cracks in mode I deviating from their initial direction of propagation). We mention that the proposed criterion is directly applicable to mixed-mode crack propagation by adding the mode II terms in the elastic solution at the crack-tip—from Freund (1998) for instance, and the direction of propagation will be predicted. The influence of K_{II} on the direction of propagation will be coupled with the role played by the crack-tip speed and the present T -stress.

4 Validation of the role of T -stress on the crack branching in Borden's simulation benchmark

After theoretically advocating the dynamic crack instabilities, we turn into their numerical validation on the interesting benchmark proposed by Borden et al. (2012), where crack branching (an instability) occurs. The section starts with a brief introduction to the benchmark and simulation results. An emergence of a positive T -stress is then showcased before branching, even though no external loadings along the direction of crack propagation exist. This section is wrapped-up by building the (in)stability map of the material in question and superposing the crack-tip's loading history (v_c and T -stress) onto the map which would give insights not only on the branching, but also on the damage band thickening observed in the phase-field simulation before branching—as will be seen.

4.1 Benchmark

Borden et al. (2012) proposed to model a pre-notched rectangular plate loaded dynamically in tension. The geometry and boundary conditions of the problem are shown in Figure 7(a). A constant traction load of 1 MPa is applied on the top and bottom boundaries of the specimen. The other boundaries are free. It is noted that the initial crack is modelled both geometrically and by imposing a phase-field value $\alpha = 1$ (fully damaged) as Dirichlet boundary condition on the initial crack surface. The ingredients of the phase-field model and the material properties from (Borden et al. 2012) are recalled in Table 2.

Figure 7(b) shows the final damage state of the material and Figure 7(c) showcases the crack tip speeds. The following observations can be drawn:

- the crack is initiated after $t = 12 \mu\text{s}$
 - no branching occurs at the crack's maximum speed ($t = 31 \mu\text{s}$), only broadening of the damage band (until $t = 36 \mu\text{s}$)
 - the crack decelerates and two branches bifurcate at an angle $\theta_0 = \pm 25^\circ$ at $t = 48 \mu\text{s}$
- Regarding the damage band width:
- The damage band broadens from $t = 31 \mu\text{s}$ to $t = 36 \mu\text{s}$; afterwards, the crack propagates stably

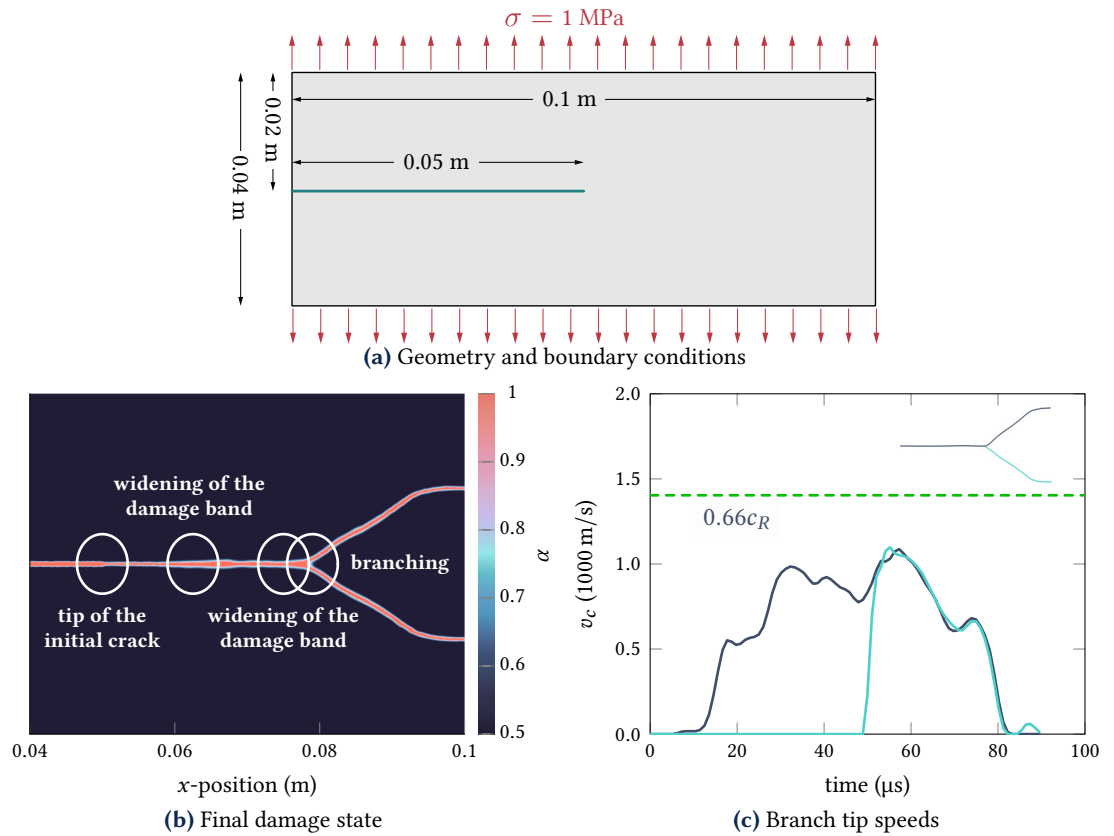


Figure 7 Crack branching benchmark from Borden et al. (2012). (a) Notch modelled both geometrically and by imposing a phase-field value $\alpha = 1$ on the notch surface (as an initial crack). (b) Final damage state. (c) Evolution of the branch tip speeds.

Time stepping	Explicit (Li et al. 2016)
Crack density function	Quadratic (Miehe et al. 2010)
Strain split	Orthogonal (Nguyen et al. 2020)
Plane strain assumption	
Boundary condition	Traction load (Figure 7(a)) (Borden et al. 2012)
E (Young's modulus)	32 GPa
ν (Poisson ratio)	0.2
ρ (Material density)	2450 kg/m ³
g_c (Material toughness)	3 J/m ²
l_c (Length-scale)	0.25 mm
c (Elastic-threshold for AT ₂)	0

Table 2 Overall phase-field model and material parameters considered for the simulation of the benchmark from (Borden et al. 2012).

- The damage band broadens from $t = 43 \mu\text{s}$ before branching at $t = 48 \mu\text{s}$.

The problem can be resumed as follows: *No external loading along the direction of crack propagation is present, yet the crack branches at relatively low crack-tip speeds.* From here, the following questions emerge:

- Why does the crack not branch at its peak speed ($t \approx 31 \mu\text{s}$)?
- Why does it branch after, at lower speeds? and finally,
- What does the broadening of the phase-field at the branching position and beforehand actually mean?

The answers to these questions are sought by analysing the angular distribution of the stresses along the crack propagation and analysing the (in)stabilities (from the notch until the branching point).

Remark 6 We note that the widening of the damage band before the moment of branching is similar to other phase-field simulations reported in Borden et al. (2012); Schlüter et al. (2014), and to non-local

integral damage model (Pereira et al. 2017). From a more physical point of view, this widening of the damage band could be the signature of the roughening of the crack surfaces experimentally observed to occur prior to branching (Ramulu and Kobayashi 1985). In phase-field models, Bleyer and Molinari (2017) showed how the micro-branching process is indeed a three-dimensional instability and is directly linked to surface patterns observed prior to macro-branching (Sharon and Fineberg 1996).

4.2 (In)stability analysis

The proposed methodology to analyse the dynamic (in)stabilities should stand both numerically and experimentally. In fact, having full-field measurement of the kinematics (from numerical simulations, or their estimations from DIC algorithms in the experimental application), one can estimate the crack-tip position (and crack-tip velocity v_c), the SIF and higher-order terms (e.g., T -stress), automatically following (Roux and Hild 2006; Roux et al. 2009). In brief, by projecting the displacement fields in a zone of *arbitrary* size around the crack-tip on the analytical solution of the displacements (Williams 1957), the relevant quantities relative to fracture can be estimated. The methodology is detailed in Appendix B for interested readers.

On the considered benchmark, the extraction (SIF, T -stress, v_c) holds solely between the moment of crack initiation (around $t = 12 \mu\text{s}$) and the moment of branching around $48 \mu\text{s}$. Afterwards, a redistribution of the stress states occurs due to the coexistence of two neighbouring crack-tips and the extraction become erroneous. We note that a quasi-static solution (Williams 1957; Roux and Hild 2006; Roux et al. 2009) for the projection space is considered; as the crack tip-speeds are not significantly large, the induced error from considering the quasi-static solution instead of the more complex dynamic one is marginal as the effect of crack-tip speeds increase or decrease.

The estimated crack-tip velocities v_c , K_{ID} and T -stress can then be injected into the elastodynamics solution of the stress-field in the vicinity of the moving crack-tip (Freund 1998). The fracture direction $\pm\theta_0$ can be subsequently computed for each frame of the advancing crack, based on the criterion of maximum circumferential stress. The scheme of analysis is summarised as follows: $\mathbf{u} \rightarrow \text{SIF}, T\text{-stress}, \text{crack-tip position}, \text{and } v_c \rightarrow r_c \rightarrow \boldsymbol{\sigma} \text{ and } \theta_0$.

4.2.1 SIF, T -stress and crack-tip speed v_c

The first step of the application scheme requires the evaluation of SIF, T -stress and the crack-tip speed v_c . Multiple extraction zone sizes (see Appendix B) are considered to validate the robustness of the extraction and accurately evaluate the relevant quantities. The results are shown in Figure 8. From $x = 0.05 \text{ m}$ to the position of branching, both K_{ID} and T -stress are increasing but

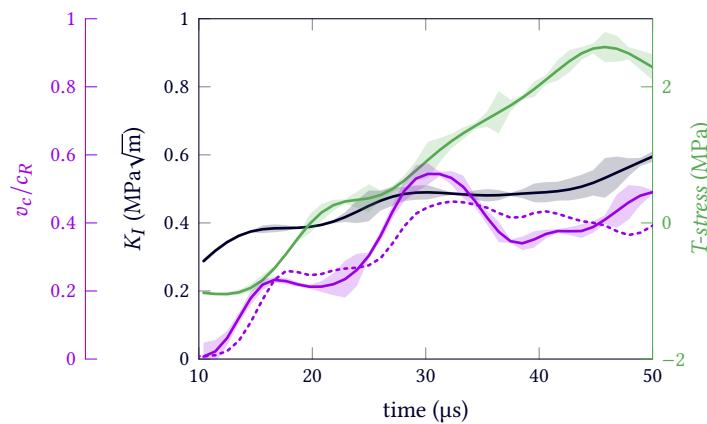
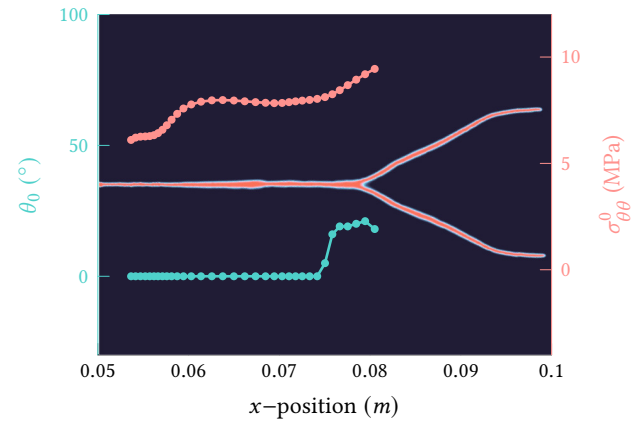


Figure 8 SIF, the higher-order term T -stress and the crack-tip speed estimated using (Borden et al. 2012)'s benchmark. The error-bar corresponds to the sensibility to the projection zone (size of the zone around the crack tip in which the analytical solution is supposedly accurate, see Appendix B). The crack-tip speed v_c^p corresponds to the speed reported in Figure 7(c) computed from the phase-field.

the crack-tip speed is oscillating. A peak in the crack-tip velocity is found at $t = 31 \mu\text{s}$. The

Figure 9 Predicted circumferential stress $\sigma_{\theta\theta}^0$ and fracture direction θ_0 along the crack propagation of the benchmark proposed in (Borden et al. 2012).



errorbar shows inaccuracy of the extraction results (K_{ID} , T -stress, and crack-tip speed) after $t = 50 \mu\text{s}$, suggesting that the branching may have occurred around this time step.²

To adequately assess the influence of T -stress on the angular stress distribution, the critical distance r_c should be determined next.

The sample's critical distance r_c can be obtained by computing r_o^{inst} as being r_o (Ramulu and Kobayashi 1983) at the supposed branching frame, and setting the (in)stability condition $r_c = r_o^{\text{inst}}$. Since $r_c = r_o$ sets the limit of instability, one can foresee that for any $r_o \geq r_o^{\text{inst}} = r_c$, the propagation is also unstable so $r_c = r_o^{\text{inst}}$ should be a first candidate at estimating r_c . r_c can then be manually optimised (trial and error) to accurately predict the actual branching angles in the simulation. Since the phase-field modelling does not explicitly represent the crack (regularisation of the discontinuity), the exact frame of branching cannot be accurately determined, this might lead to slightly inaccurate predictions of r_c . As previously mentioned, in phase-field models, branching might be preceded by a widening of the damage band (Borden et al. 2012; Schlüter et al. 2014), this widening starts earlier (earlier than the time the branches are detected). The computation of the critical distance r_c for instabilities at the moment of damage band broadening just before branching seems a reasonable speculation, it estimates r_c around $600 \mu\text{m}$.

Using this value of r_c , Figure 9 shows the fracture angle θ_0 and $\sigma_{\theta\theta}^0$ along the crack propagation from the notch to its branching position. For the crack-tip between $x = 0.05 \text{ m}$ and the position of branching, the predicted fracture direction from these data is obtained in the elongation of the crack, consistently with the simulation observation (straight crack). The maximum $\sigma_{\theta\theta}^0$ stress in this region of propagation increases rapidly from 6 MPa at $v_c = 0.23c_R$ to a plateau at 8 MPa along the stable crack propagation before branching. $\sigma_{\theta\theta}^0$ increases as the direction of fracture θ_0 deviates from 0° to 25° at the branching position.

The arisen instability at this location (the increase in the maximum stress with a change in the fracture angle) induces the branching. Consistently, the estimated branched angle from the simulation is equal to $\theta = 55^\circ \approx 2\theta_0$. Branching occurs at a relatively low crack-tip speed ($v_c \approx 0.4c_R$) in the presence of a positive T -stress $\approx 1.3 \text{ MPa}$.

We have seen how adding the higher-order term T -stress in the stress solution is reflected on the *modification of the direction of crack propagation* at r_c at the *branching position* (where the crack advances at v_c lower than the threshold predicted by the classical solution) which eventually translates to branching (crack instability).

4.2.2 Material (in)stability map

After advocating the roles played by the T -stress along with v_c on crack (in)stabilities, we construct the material (in)stability map and superpose the history of the dynamic loading. The construction requires:

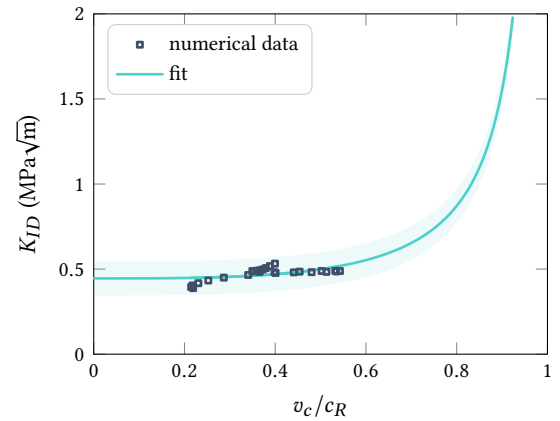
- the materials elastic properties reported in Table 2 from Borden et al. (2012)'s benchmark;
- the reference distance $r_c = 600 \mu\text{m}$ numerically computed from the application of Ramulu and Kobayashi (1983)'s criterion on SIF, T -stress and v_c as r_o at the supposed branching moment.

² From the simulation's damage field, branching is found to occur at $t = 48 \mu\text{s}$, after some widening of the damage band.

- The crack dynamic propagation law that should be determined: as the full-field kinematics provide estimates of K_{ID} and v_c , it is found that the empirical law in Equation (7) and the eventual crack-tip speeds fit well the K_{ID} and v_c data: with $K_{ID} = 0.445 \text{ MPa}\sqrt{\text{m}}$ and $m = 3.2$, see Figure 10.

Remark 7 With the absence of data-points at both low crack-tip speeds $v_c \leq 0.2c_R$ and high crack-tip speeds $v_c \geq 0.6c_R$, the validity of the fit (Figure 10) in these range is questionable. Of course, this would limit the soundness of the analysis for cracks propagating at speeds in the range $0.2c_R \leq v_c \leq 0.6c_R$, whereas this does not affect the results in this example since the analysis is lead on crack propagating within these speed ranges.

Figure 10 Numerical K_{ID} and v_c with the fit corresponding to the crack propagation behaviour law in Equation (7) and suggested by Kanninen and Popelar (1985): $K_{IC} = 0.445 \text{ MPa}\sqrt{\text{m}}$ and $m = 3.2$ are found.



The (in)stability map is given in Figure 11. The focus will be shed on the $(v_c, T\text{-stress})$ -space. The crack propagation history is superposed on the map. From the notch, the crack propagates at increasing v_c and $T\text{-stress}$. It heads towards the transition zone around $v_c = 0.54c_R$ and $T\text{-stress} = 1.07 \text{ MPa}$ at $t = 31 \mu\text{s}$. This time corresponds to the beginning of crack widening observed in Figure 7(b). The propagation history then shows a decelerating crack that would enter the transitional zone at $v_c = 0.38c_R$ and $T\text{-stress} = 2.49 \text{ MPa}$, corresponding to $t = 43 \mu\text{s}$, the time at which the damage band is observed to broaden just before its branching.

The (in)stability map also predicts that maximum stress occurs during the first widening of the damage band at $t = 31 \mu\text{s}$. Once again, the maximum value of $\sigma_{\theta\theta}^0$ herein reached does not necessarily account for crack branching as θ_0 stays null. Here, the closeness to the transition zone destabilises the crack and broadens the damage band but without inducing branching because the actual combination of K_{ID} and $T\text{-stress}$ at this stage does not lead to a deviation of θ_0 away from 0. Then as the crack propagation history curve enters the transitional zone, the damage band is observed to broadens before branching. *Having $\theta_0 \neq 0$ is a sufficient condition for branching while having the stress surpass a certain threshold is only necessary.*

5 Experimental validation of the role of $T\text{-stress}$ on crack branching in an inertial impact test

After theoretically elaborating the (in)stability criterion and validating the role played by $T\text{-stress}$ on dynamic (in)stabilities on a numerical phase-field simulation, we turn to an experimental validation on a novel experimental setup. The specimen geometry from Grégoire et al. (2007) is combined with the test configuration from Pierron et al. (2014) to enable interesting crack propagation interaction with stress-waves; knowingly:

- compressive waves from the impact are converted to tensile ones and initiate the crack propagation;
- the propagating crack meets reflected stress-waves from the boundaries and bifurcates into two symmetric branches.
- the two branches propagate at similar velocities and along similar symmetrical paths.

All these phenomena and more will be investigated in details.

The available cutting edge technologies (gas gun, UHS-HR camera) combined with advanced

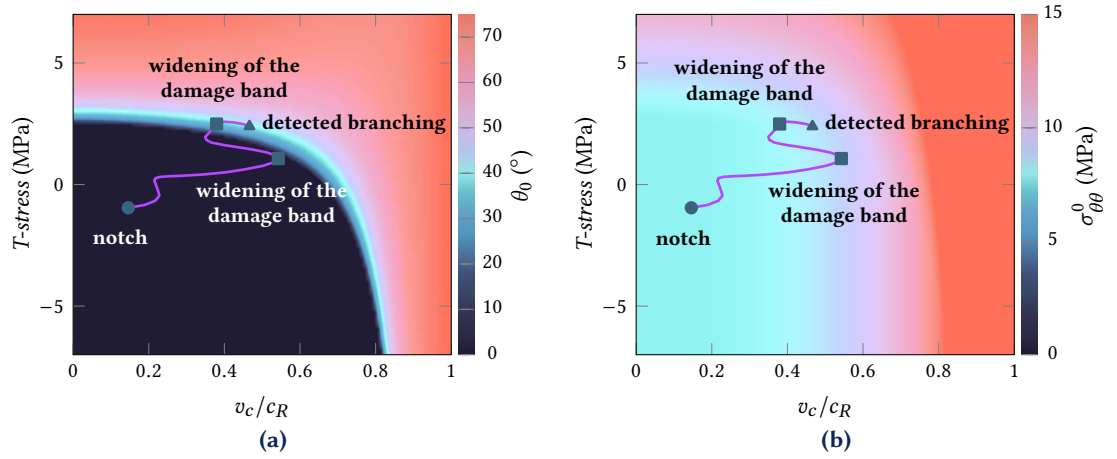


Figure 11 (In)stability and maximum circumferential stress maps of the benchmark, constructed from Borden’s simulation results. The history of the propagation is shown in purple, the initiation from the notch (circular marker), the two widenings of the damage band (square markers), and the branching (upward-pointing arrow) are all reported on the maps.

DIC skills³ (in-lab-developed state-of-the-art calibration methodology (Vinel et al. 2021)), at École Centrale de Nantes, enabled the investigation on advanced experimental configurations inspired from (Pierron et al. 2014) and (Grégoire et al. 2007) where full-field measurements of a high-velocity impact test (~ 30 m/s) are exploited to extract meaningful fracture mechanics quantities (SIF, T -stress, crack-tip position, crack-tip speeds, etc.) and to analyse the dynamic fracture behaviour.

5.1 Loading and test configuration

The specimen shown in Figure 12 is to be loaded dynamically via an impact on the edge perpendicular to the notch as schematised in Figure 13. The specimen is mounted on a waveguide

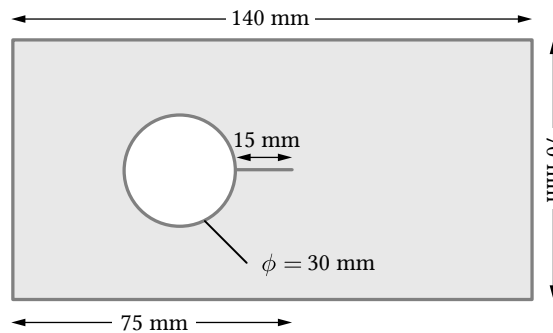


Figure 12 Sample geometry and dimensions for the inertial impact test (Grégoire et al. 2007). The hole converts the compressive wave from the input to a tensile loading at the notch.

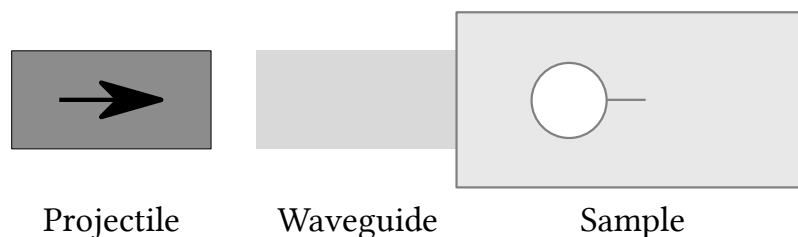


Figure 13 Schematic representation of the experimental configuration.

to ensure proper compressive wave entering the specimen (Van Blitterswyk et al. 2018; Vinel et al.

³ The open-source in-lab-developed software UFreckles is available at the permalink <https://zenodo.org/record/1433776>.

2021), and to hold the sample while keeping all other boundaries free. The impact should induce a compressive wave; however, the presence of the hole creates a tensile zone sideways opening thus the notch and enabling the fracture initiation (Grégoire et al. 2007). As compared to Grégoire et al. (2007)’s work, the absence of an impedance at the right-hand side boundary (in his case, the use of Hopkinson’s bars with similar mechanical properties to those of the specimen), stress-waves will be fully reflected from the right-hand side boundary and will deliver new loading-unloading conditions of the crack-tip probably modifying its advancement, as will be seen shortly.

5.2 Experimental and imaging setup

The sample is laser-cut from a commercial PolyMethyl Methacrylate (PMMA) manufactured by Arkema. The laser’s beam diameter ($d_{\text{laser}} = 200 \mu\text{m}$) is taken into account for the dimensioning. The pre-crack’s width matches the beam’s. A synthetic speckle pattern is laser-engraved onto the sample surface following (Vinel et al. 2021) (useful for ensuring quality and reproducibility of the pattern for the application of the DIC procedure). The projectile and the waveguide are both machined from a polyoxymethylene (POM) cylinder of diameter $d_{\text{proj}} = d_{\text{wg}} = 40 \text{ mm}$; both are 80 mm long. POM is used because it has similar material properties as PMMA (regarding the speeds of elastic waves). The specimen is mounted to the waveguide ③ with the help of a machined sleeve. It is then glued before removing the sleeve. The ensemble (specimen-waveguide) is systematically positioned on a PMMA support bed at the end of the gun (on optical positioners ④) to secure the proper alignment with the projectile at the moment of impact. A projectile is fired by a gas gun ① to reach a velocity of V_{proj} just before the impact (impact with the waveguide on which the specimen is mounted). The sudden expansion of the gas inside the barrels is what impels the projectile towards the waveguide.

All images are captured using the UHS-HR Cordin Model 580 ⑥ (at 400 kfps with a resolution of $3296 \times 2472 \text{ pix}$). At such ultra high speed and high resolution, the camera records the entire test: from the first compressive waves induced by the impact to the total failure of the specimen (about $200 \mu\text{s}$, 78 frames). Two Pro-10 Profoto flashes ⑤ ($2 \times 2400 \text{ J}$ provided in $1000 \mu\text{s}$) provide enough lighting for the camera sensors.

A schematic graph of the triggering of the camera and flashes is plotted in Figure 14. The

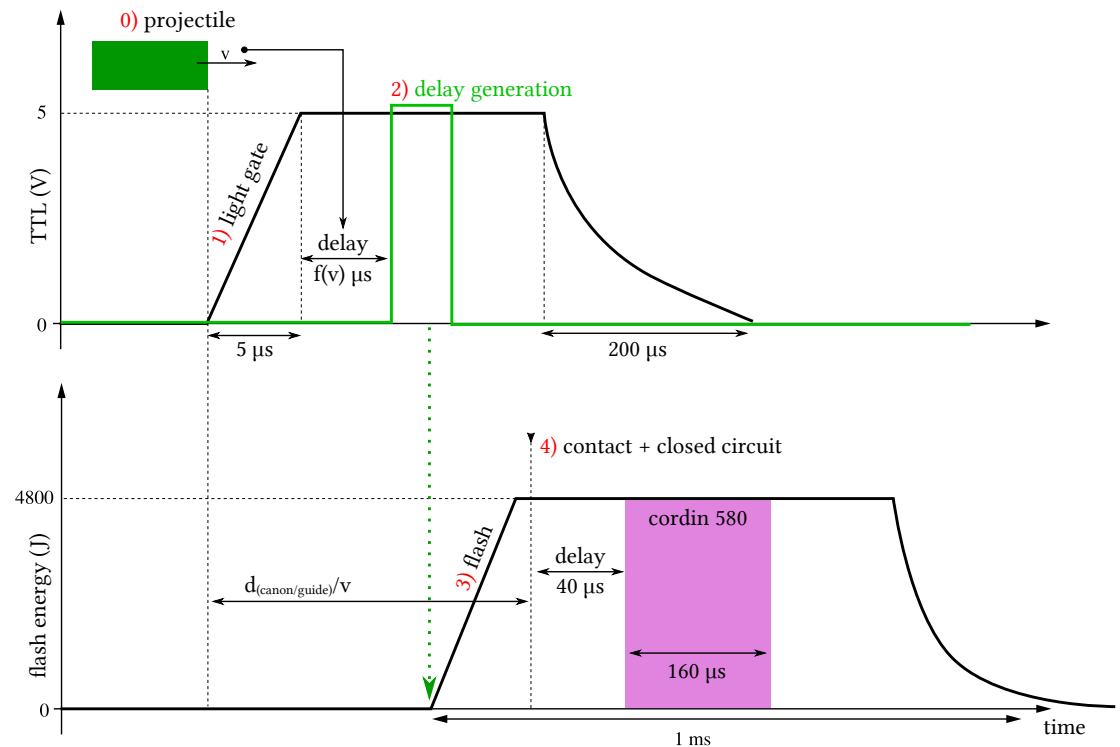


Figure 14 Imaging setup: automatic triggering of the camera and the flashes.

flashes are triggered via an infrared light-gate system (SPX1189 series Honeywell) ⑦ mounted at the end of the gas gun ①. When obscured by the projectile ①, it sends a 5 V TTL signal

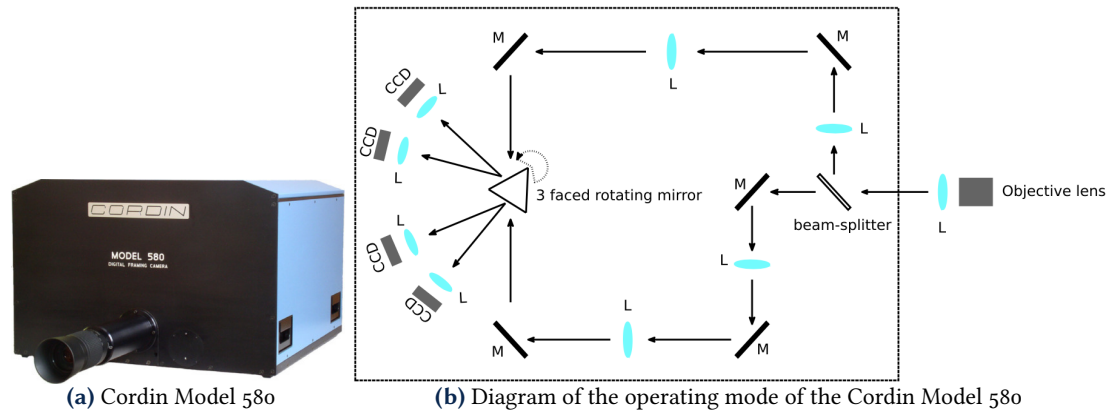


Figure 15 The Cordin Model 580 and its operating mode. L: Lens, M: Mirror, CCD: CCD sensors (Vinel et al. 2021).

1) (rise time = 5 μs). The signal is then delayed by 200 μs 2) via a delay generator ⑧ before igniting the flashes 3). The delay takes into account for the air-travel time of the projectile (from the outlet of the gas gun to the impact) + the time it takes the stress waves induced in the waveguide to reach the specimen – the warm-up time of the flashes, see Figure 14. An aluminum film is bonded onto the projectile. Two pieces of aluminum film are bonded onto the waveguide ③ and connected to a circuit (open) between a 5V generator and the camera trigger ⑥, so that when the projectile hits the waveguide, it contacts 4) both pieces of film closing thus the circuit and providing the triggering signal for the camera. The camera is then triggered with a delay of 40 μs (delay generator ⑧), which corresponds to the time the stress waves (generated at the impact with the projectile) take to reach the boundary of the specimen through the waveguide.

On the operating mode of the Cordin Model 580 UHS-HR camera: the light beam, represented by the black arrows in Figure 15, enters the camera through its objective lens. It then encounters a cubic beam splitter which will either transmit the light or reflect it at a 45° angle. The light is then reflected off mirrors until it hits a lens. After this lens, another mirror reflects the light beam onto a three-sided rotating mirror. Finally, the light passes through a lens, used to attenuate the bias induced by the rotation of the mirror on the exposure time of the individual sensor, and finally reaches the sensor.

Such an exotic multi-sensor technology provides a combined temporal-spatial resolution (up to 4 Mfps at 8 Mpix) and recording length (78 images) that are simply *unreachable* for other technologies. Such a resolution gain is of prime interest when investigating fracture mechanics problems; nevertheless, it comes at a cost of complex optical distortions (3 × 78 independent lens-mirror-sensor combinations) and varying image sharpness (due to varying beam angle with respect to the rotating mirror). Main parts of the bias can be cancelled-out using the in-house developed calibration method detailed in (Vinel et al. 2021). Despite the application of the calibration, DIC results still come with sub-pixel uncertainty levels one order of magnitude higher than the standards with classical cameras (around 10⁻¹ pixels compared to 10⁻² in the standard cameras). Table 3 summarises the overall DIC parameters.

A photo of the test bench can be found in Figure 16. One identifies ① the gas gun, ② the

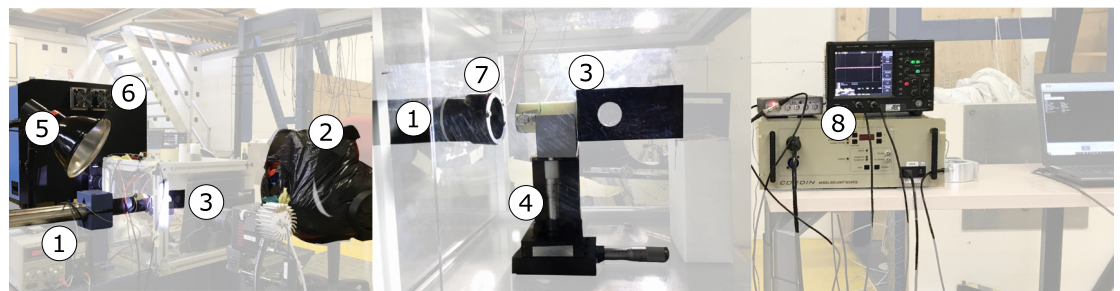


Figure 16 Experimental set-up for the inertial impact tests.

shock absorber, ③ the specimen mounted on the waveguide, ④ the PMMA support bed on the

optical positioners, ⑤ the flash lights, ⑥ the Cordin Model 580 UHS-HR camera, ⑦ a light-gate: the SPX1189 series Honeywell infrared sensor, and ⑧ the delay generator.

Camera	Cordin Model 580
Image resolution	3296 × 2472 pix
Dynamic range	Detector 12 bits
Acquisition rate	400 kfps
Lens	Tamron SP 90 mm Di Marco
Aperature	$f/2.8$
Field of view	154.25 mm × 115.69 mm
Image scale	1 pix = 0.0468 mm
Patterning technique	Laser etching of a synthetic speckle (Vinel et al. 2021)
DIC software	Ufreckles (https://zenodo.org/record/1433776)
Shape function	T3P1 linear triangular elements
Metric	Element-wise ZNSSD
Data processing	Tikhonov regularisation (over 3 elements)
Data post-processing	Temporal Savitzky Golay filter (kernel size = 5 frames, order 2)
Experimental uncertainty (Vinel et al. 2021)	U_{DIC} : ±0.2 pix (displacement) ϵ_{DIC} : ±2 mε (strain) $\dot{\epsilon}_{DIC}$: ±50 s ⁻¹ (strain rate)

Table 3 DIC parameters.

A series of impact tests in Figure 16 were performed at Ecole Centrale de Nantes. Four representative samples are analysed (designated TAF1, TAF2, T3DE and THOM). Only results and full-field measurements of the TAF1 sample will be detailed. Related material to TAF2, T3DE and THOM are showcased in Appendices A.1 to A.3, respectively.

5.3 Post-mortem state of the sample

By carefully setting the gas guns pressure to 1.49 atm and 1.55 atm, the projectile's speed⁴ just before the impact was respectively around 20 m/s and 30 m/s (22 m/s for TAF2 and THOM, 30.5 m/s for TAF1, and 31.8 m/s for T3DE).

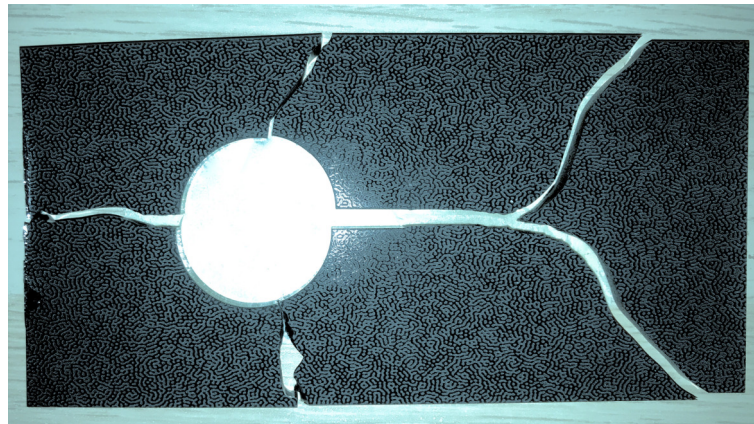


Figure 17 Post-mortem photograph of sample TAF1 with impact velocity $V_{proj} = 30.5$ m/s.

Figure 17 shows the crack(s) paths on the sample TAF1 (*post-mortem*). As seen, a crack is observed at the left-hand side of the hole. Undoubtedly, Poisson effect coming from the horizontal compression is responsible for the initiation. A little curve on the crack suggests a small misalignment in the mounting of the specimen on the waveguide, or between the waveguide and the projectile. On the right, a crack is initiated from the notch, it travels horizontally (24 mm) before branching into two branches (at an angle $\theta = +40^\circ$ and $\theta = -15^\circ$). Each branch displays two convexities; stress-wave reflection at the free boundaries are expected to play a predominant

⁴ The projectile's speed is computed from images taken at the lower frame rate 10 000 fps with a standard high-speed camera.

role on these deviations. Two vertical cracks are also present at the top and the bottom of the hole.

The samples consistently show the same crack patterns (Appendix A.1 for TAF2 and Appendix A.2 for T3DE) suggesting a repeatability of the setup, and interesting phenomena waiting to be explored.

Highly resolved ultrafast imaging combined with DIC enables the validation of the big role played by the stress-waves on the cracks patterns, but before exploring the measurements, we give some pertinent remarks regarding the DIC data processing:

Remark 8 The displacement fields are filtered in time with a Savitzky Golay (kernel size = 5 frames, order 2) filter to smoothen the first derivative (velocity fields); moreover, spatial noise is filtered out via a Tikhonov regularisation of the DIC problem (with a cut-off wavelength $60 \text{ pix} = 3 \times$ the finite element size of the DIC mesh).

Remark 9 The strain-rate fields are derived by spatial differentiation of the velocities; velocities are derived from temporal differentiation of time-filtered displacement fields.

Remark 10 The time origin ($t = 0$) corresponds to the camera trigger.

5.4 DIC displacement fields

An unstructured mesh with twin nodes along the crack path is considered for the DIC problem on each specimen (following (Vinel et al. 2021)). Figure 18 shows the unstructured mesh (in blue) deformed and superimposed onto the final frame taken during an impact test. The use of twin nodes in the mesh allows the opening of the latter thus correctly capturing the jumps of displacement at the lips of the crack(s). The construction of such mesh is a two-step procedure, interested readers are referred to (Vinel et al. 2021; Réthoré et al. 2008) for further details.

Remark 11 Crack-tip speed can be calculated from the opening of the crack lips along the crack path (twin nodes along the crack path). Figure 20 showcases the tip-speeds of the two main cracks (on the left and right-hand sides of the holes) and of the branch. Details regarding the crack-tip speeds are discussed in the next section. The apparent speed computed from the opening of the twin nodes along the crack path is only a rough estimation of the actual crack-tip speed since it can be affected by local noise, lighting of the crack lips and pixel resolution. A more precise estimation is to be evaluated using Roux and Hild (2006); Roux et al. (2009)'s projection method.

Figure 18 DIC finite-element mesh for the TAF1 specimen; mesh size: 20 – 32 pix per element.

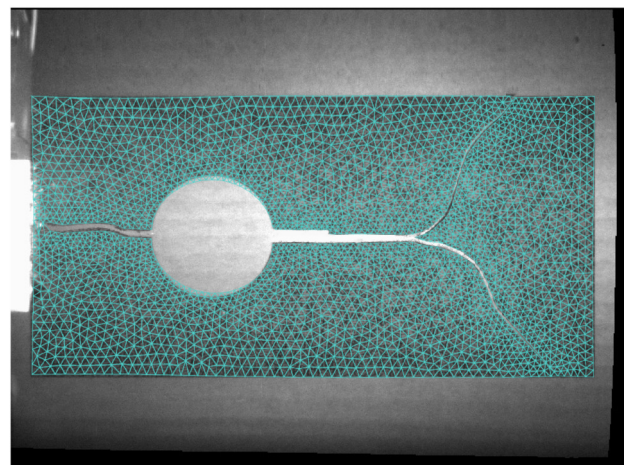


Figure 19 shows displacement fields, longitudinal and transverse strain rate fields of the TAF1 specimen at three different time steps. The following phenomena occur around these time steps: at $10 \mu\text{s}$ (figures on the left), the first stress-waves entering the specimen are shown, at $60 \mu\text{s}$ (figures in the middle), the crack on the right-hand side of the hole is initiated from the notch, at $95 \mu\text{s}$ (figures on the right), the crack bifurcates into two branches. For the other specimens, see Appendices A.1 to A.3.

Remark 12 The initiation and the bifurcation frames are determined from the opening of the crack lips (twin nodes along the crack path) in the images from the UHS-HR camera.

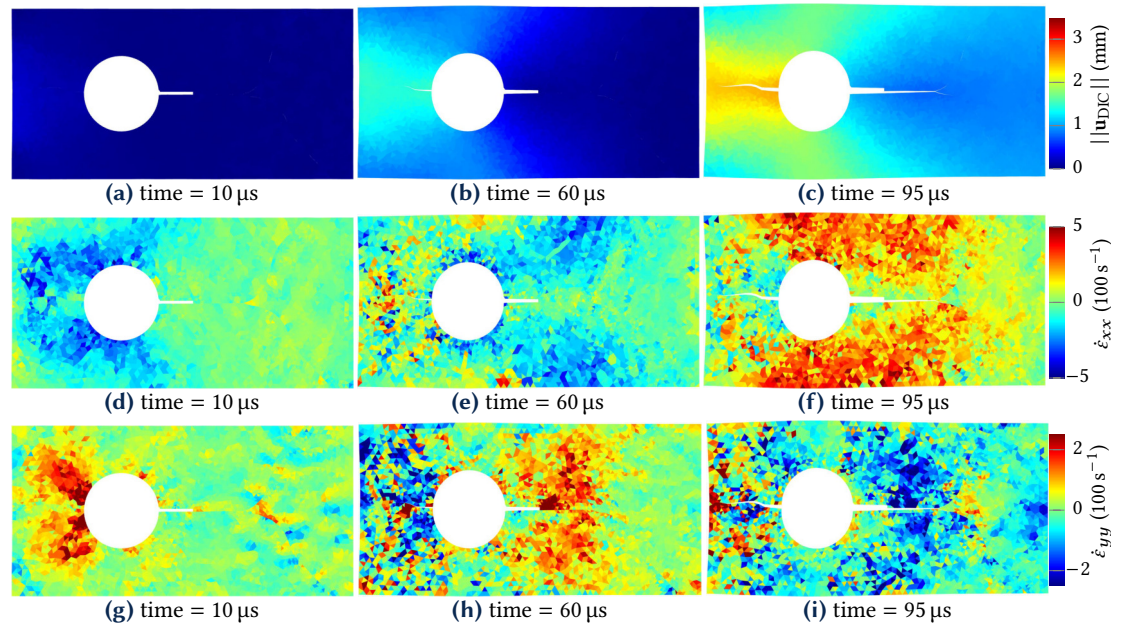
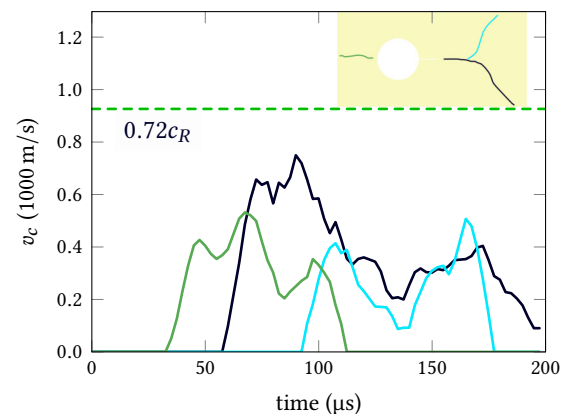


Figure 19 Sample TAF₁-DIC displacement fields (top), longitudinal (middle) and transversal (bottom) strain rates at three time steps. A Savitzky Golay (kernel size = 5 frames, order 2) filter smoothens the velocity fields. Spatial noise is filtered-out via a Tikhonov regularisation of the DIC problem.

Figure 20 Experimental apparent crack-tip speeds of TAF₁ sample obtained from the crack opening.



The ability to register 78 snapshots at 400 kfps enables capturing never-seen-before details regarding stress-wave and crack propagation. The apparent crack-tip speeds (calculated from the crack opening) are shown in Figure 20. The most compelling phenomena are listed under ►.

- The initiation of the impact and the first compressive waves enter the specimen (at 500 s^{-1} strain-rates, shown at $t = 10 \mu\text{s}$ in Figure 19(d));
- The role of the hole in creating traction zones sideways at $t = 10 \mu\text{s}$ in Figure 19(g). As seen in the previous Section 5.3, two main cracks are observed sideways of the hole (a first one at left-hand side of the hole and another one from the notch). Observation from the DIC displacement fields show that *surprisingly*,
- the crack at the left-hand side of the hole is first initiated ($t = 40 \mu\text{s}$). Once its length reaches 15 mm,
- the second crack initiates from the notch at the right-hand side of the hole (at around $t = 60 \mu\text{s}$). After initiating from the notch around $t = 60 \mu\text{s}$, the crack accelerates to roughly 700 m/s corresponding to $0.55c_R$, see Figure 20.
- Compressive stress-waves are reflected as traction waves from the right-hand side boundary, and they overlap the tip of the crack.

The crack decelerates and reaches the branching position while travelling at around $v_c = 650 \text{ m/s} = 0.5c_R$, see Figure 20.

- ▶ Bifurcation of the crack into two branches happen at $t = 95 \mu\text{s}$.
- ▶ The two branches advance at very similar velocities, see Figure 20.
- ▶ Complex stress-wave orthogonal to the crack branches supposedly deviate the branches.

Even though the same geometry as in Grégoire et al. (2007)'s work is used, it is clear that the stress-wave propagation history is fundamentally different (the absence of an impedance at the right-hand side of the specimen). Stress-wave reflections from the right-hand side boundary deliver new loading-unloading events of the crack-tip, which indeed enables distinctive crack patterns. Also, the higher impact velocity can be related to the higher level of energy transmitted to the specimen yielding the formation of several fragments (due to crack branching).

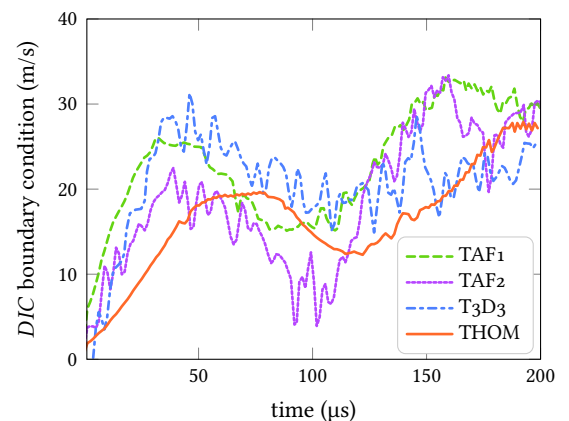
5.5 (In)stability analysis

The ability to quantify the rich dynamical behaviour of the cracks (initiation, acceleration, deceleration, branching) was enabled thanks to the novel experimental setup and the advanced DIC skills. The focus is shed on the branching phenomenon. As observed, the branching occurs after a certain duration of time in which the main crack appears to be decelerating. Questions regarding the presence of a *limiting velocity* from one side and regarding the crack *branching at lower crack-tip speeds* from the other are asked. To this end, we follow the application scheme previously proposed and numerically validated: It starts by estimating the *SIF*, *T-stress*, the crack-tip position and the crack-tip speed v_c from the experimental full-field kinematics following. And it is followed by determining r_c which enables the assessment of the angular distribution of the stresses along the crack propagation (between the notch and the branching position).

We start by showcasing the *SIF*, *T-stress* and crack-tip speed results computed directly from the DIC displacement fields, as intermediate results from the analysis scheme. The elastic properties of the PMMA specimen are required to be known to estimate these quantities (Roux and Hild 2006; Roux et al. 2009). The elasticity tensor is determined via an *in-house FEMU* (Finite Element Model Updating Method) identification method. Even though PMMA exhibits viscoelastic material properties, it is hard to identify the effective viscoelastic parameters due to the complexity of loading and unloading (inertial effects). From here, it is assumed that the samples exhibit linear elastic behaviour, with a modification on the elastic properties (as compared to the quasi-static properties) to take the global strain-rate effects into account.

To build the identification problem for the FEMU, several numerical dynamic simulations are launched having as boundary conditions the longitudinal and transverse displacements of the nodes of the mesh at the edge impacted, obtained through the DIC measurements. Figure 21 shows the average longitudinal velocity of the nodes of the impacted edge of the samples TAF1, TAF2, TAF3 and THOM. Note how the impact velocity of the projectile found previously (22 m/s for TAF2, 30.5 m/s for TAF1, 31.8 m/s for T3DE and 22 m/s for THOM) is reflected on the edge velocity of each. The simulations are stopped just before any crack initiation. The simulated

Figure 21 Experimentally measured velocities at the boundary (average velocity of the boundary nodes at each frame measured from DIC is shown) applied as a boundary condition in the numerical simulations for the identification of the elastic parameter taking into account the global viscoelasticity strain-rate effect.



displacement fields \mathbf{u}_{sim} and those experimentally measured \mathbf{u}_{DIC} are then compared, and we

write

$$F_{\text{obj}}^{\text{vis}} = \sum_{t=0}^{t=t_i} |\mathbf{u}_{\text{DIC}}(t) - \mathbf{u}_{\text{sim}}(t, \mathbf{C}_v)|^2. \quad (8)$$

The minimisation of the objective function in Equation (8) gives the isotropic elasticity tensor \mathbf{C}_v which best reproduces the global response of the material. From \mathbf{C}_v , and assuming plane strains, we obtain a Young modulus $E = 6$ GPa and a Poisson ratio $\nu = 0.3$. Table 4 summarises the identified material properties under the plain strain assumption.

ρ	E	ν	c_s	c_R	c_d
1200 kg/m ³	6 GPa	0.3	1387 m/s	1287 m/s	2594 m/s

Table 4 Material properties for the PMMA identified from the full-field measurements via the in-house FEMU identification method.

5.5.1 SIF, T -stress and crack-tip speed

Figure 22 shows the extraction results, namely SIF, T -stress and the crack-tip speed v_c . The robustness of the extraction (vis-à-vis its parameter, i.e. sizes of extraction zones, see Appendix B) is also reported by the error-bars. The following observations can be drawn:

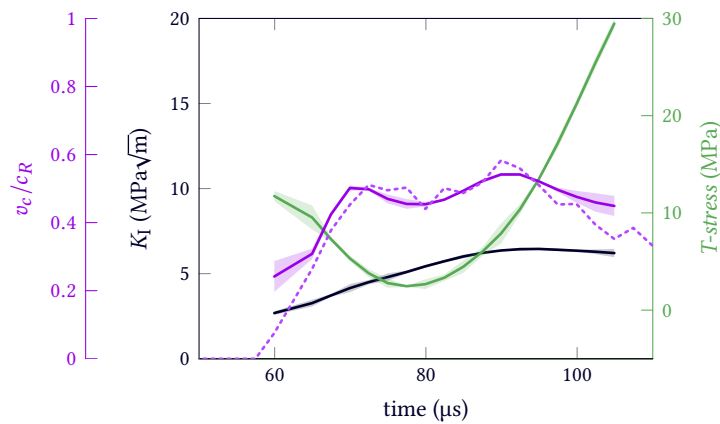


Figure 22 Experimental SIF, the higher-order term T -stress and the crack-tip speed in TAF1 sample. The error-bar corresponds to the sensibility to the extraction zone (Roux and Hild 2006; Roux et al. 2009), the crack-tip speed v_c^o corresponds to the one reported in Figure 20 (computed from the crack opening). Crack branching occurs around $t = 95$ μs .

- ▶ From $t = 60$ μs (crack initiation from the notch) to $t = 95$ μs , K_{ID} increases from $K_{\text{ID}} \approx 2.68$ $\text{MPa}\sqrt{\text{m}}$ to a plateau at $K_{\text{ID}} \approx 6$ $\text{MPa}\sqrt{\text{m}}$.
- ▶ The velocity of the elastic crack-tip on the other hand reaches a plateau around $v_c = 0.5c_R$ at $t = 70$ μs , oscillations around this plateau are observed and the maximum velocity $v_c = 0.55c_R$ is reached at 90 μs . Afterwards, the crack-tip starts decelerating until it reaches $v_c \approx 0.52c_R$ at the moment of branching, around $t = 95$ μs .
- ▶ Regarding the first higher-order term, knowingly the T -stress, an initial decrease is observed from 11 MPa initially to a minimum of T -stress = 2.46 MPa at $t = 77$ μs . Afterwards, T -stress rockets through T -stress = 13.46 MPa at the moment of branching.

The rapid increase of T -stress before the crack branching echoes the tensile stress-wave reflected from the right-hand side boundary, as observed in Figure 19 and discussed in Section 5.4. The increase of T -stress before branching is also observed in TAF2, T3DE and THOM samples.

Since the DIC provides good estimates of the frame (\pm one frame) at which the branching occurs, the sample's critical distance r_c can again be obtained by computing r_o^{inst} as being r_o at the branching frame, and setting the (in)stability condition $r_c = r_o^{\text{inst}}$. The value $r_c = 2 \pm 0.16$ mm is consistently found across the four experiments, which proves it to be a material constant as

previously preconised (Rice and Johnson 1970; Ritchie et al. 1973; Ramulu and Kobayashi 1983). The identification is directly obtained from $r_c = r_o^{\text{inst}}$ without manual optimisation.

The evolution of the direction $\pm\theta_0$ at different positions of the crack-tip inside the material is reported in Figure 23. From the trend of θ_0 , it is clear how:

- ▶ the fracture direction is always along the crack growth from the notch till before the branching position;
- ▶ at the branching position, the direction of propagation is accurately predicted by the change of θ_0 (increase from $\theta_0 \approx \pm 0$ to $\pm 10^\circ$ and then to $\pm 32^\circ$);
- ▶ $\sigma_{\theta\theta}^0$ increases and reaches a plateau around 55 MPa before branching.

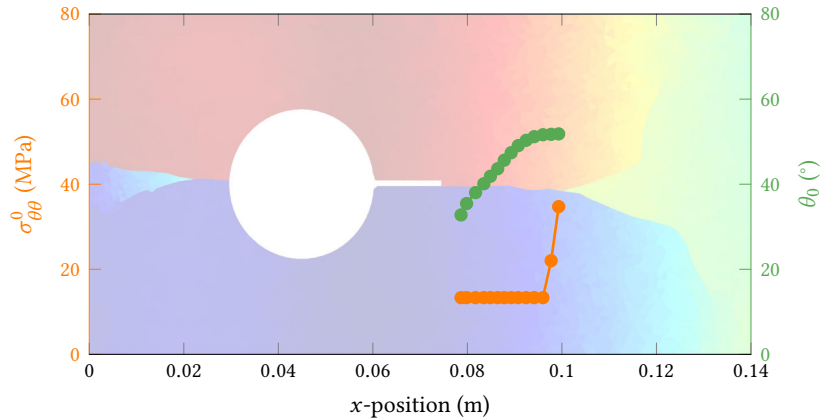


Figure 23 Evolution of the predicted fracture direction θ_0 along with the maximum circumferential stress computed at $r_c = 2$ mm in TAF1 sample (SIF, T -stress and v_c from DIC experimental fields). The modification of the fracture angle θ_0 at the position of branching and the evolution of $\sigma_{\theta\theta}^0$ mirror the experimental branching.

5.5.2 General results of the four samples

The following observations are drawn from the analysis of the samples TAF1, TAF2, T3DE and THOM:

- ▶ For the four samples, the maximum circumferential stress before branching reaches 55 ± 8 MPa.
- ▶ The branching angles are reflected on the change in the direction of fracture θ_0 at the branching position; at velocities around $v_c = 0.52c_R$ for TAF1 and T3DE, and around $v_c = 0.4c_R$ for TAF2 and THOM.
- ▶ $r_c = 2 \pm 0.16$ mm is consistently found across the four experiments.

Hence the unquestionable role played by T -stress on the branching instability at relatively low crack-tip speeds ($v_c = 0.4 - 0.52c_R$) is experimentally highlighted thanks to the advanced imaging and experimental technologies.

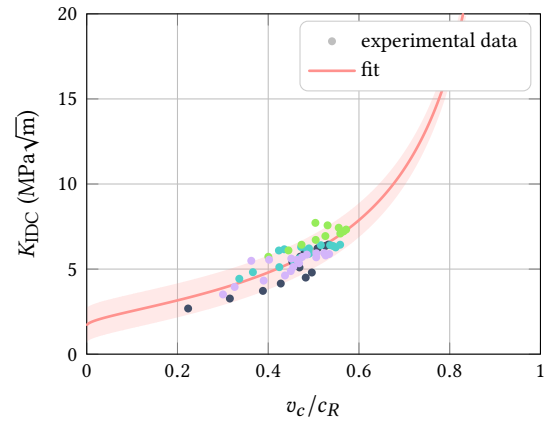
5.5.3 Experimental (in)stability map of PMMA

After putting-forth the unquestionable role of T -stress on crack (in)stability, we wrap-up this experiential study by constructing the PMMA (in)stability map *solely* from experimental findings. The materials elastic properties are experimentally determined via the in-house FEMU and reported in Table 4; then, the material constant r_c is experimentally computed from the application of Ramulu and Kobayashi (1983)'s criterion on SIF, T -stress and v_c information from full-field measurements. Finally, the full-field measurements provide SIF and v_c data on the relationship between the stress intensity factor and the velocity of the crack-tip. Assuming that the crack advances at $K_{\text{IDC}} = K_{\text{ID}}$, where K_{ID} is the instantaneous dynamic stress intensity factor estimated from full-field measurements, it is found that the empirical law in Equation (7) fits well the experimental data.

Figure 24 shows the behaviour law of the crack propagation fitted on data from the four samples. The determined parameters $K_{\text{IC}} = 1.66 \text{ MPa}\sqrt{\text{m}}$ and $m = 0.465$ accurately portray the dynamic crack propagation behaviour in the PMMA samples.

With all the required information, the material (in)stability map is constructed and showcased

Figure 24 Experimental K_{ID} and v_c (circular markers) with the fit corresponding to the crack propagation behaviour law following Kanninen and Popelar (1985) $K_{IC} = 1.66 \text{ MPa}\sqrt{\text{m}}$ and $m = 0.465$ are found, the colours corresponds to experimental data from the different samples.

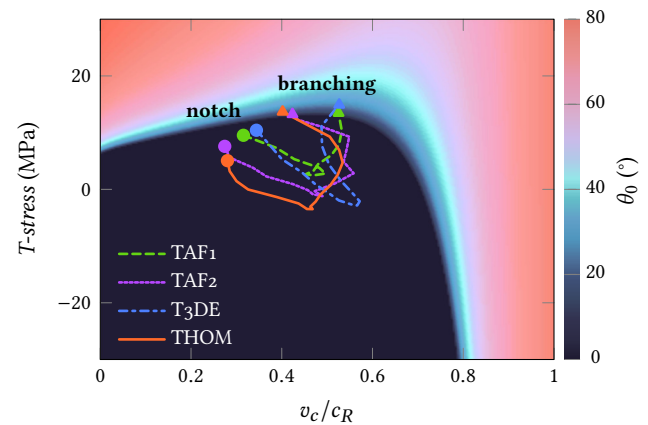


in Figure 25 in the $(v_c, T\text{-stress})$ -space. We analyse an arbitrary range of $T\text{-stress}$ between -30 MPa and $+30 \text{ MPa}$.

5.5.4 Experimental crack-tip-loading paths

The history of the crack propagation from the notch until its branching for the 4 samples are displayed in Figure 25. The circular marker on the curves corresponds to the (frame ± 1 frame) at

Figure 25 (In)stability map of PMMA constructed from experimental measurements and fitted to Kanninen and Popelar (1985)'s empirical law. The history of the crack propagation in each sample is displayed. From the initiation at the notch (disc marker) until the branching position (triangle marker) ± 1 frame, the map accurately predicts the (in)stability at the branching position with the change of θ_0 .



which the crack initiates from the notch (usually most south-west point in these experiments) and the arrowhead corresponds to the frame at which the crack branches (± 1 frame) (usually most north-east point in these experiments).

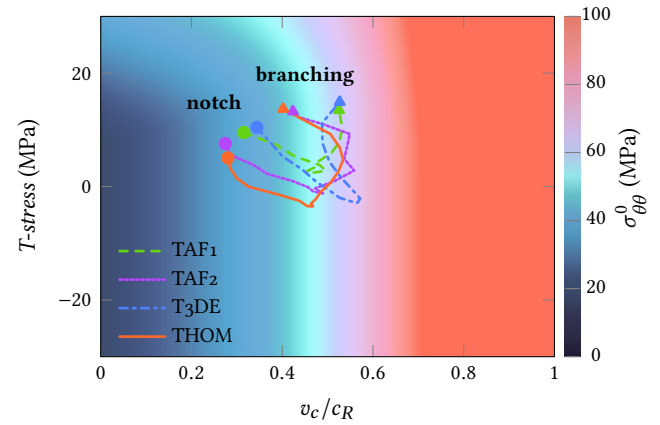
In the $(v_c, T\text{-stress})$ -space, the four growth patterns are similar, where a decrease in $T\text{-stress}$ with an accelerating crack are observed followed by a increase in $T\text{-stress}$. Two different crack propagation behaviours are observed for two couples of samples (TAF1 and T3DE from one side, TAF2 and THOM from the other):

- the cracks TAF1 and T3DE branch at $v_c = 0.52 \pm 0.0002c_R$ in the presence of a $T\text{-stress} = 14.23 \pm 1 \text{ MPa}$;
- the cracks TAF2 and THOM branch at lower crack-tip speeds $v_c = 0.41 \pm 0.1c_R$, in the presence of a $T\text{-stress} = 13.46 \pm 0.3 \text{ MPa}$.

Remark 13 The similarity in the crack scenarios (by pair) is probably due to the fact that the impact velocities, see Section 5.3, are similar for TAF1 and T3DE ($V_{\text{proj}} = 30.5 \text{ m/s}$ and 31.8 m/s) from one side, and for TAF2 and THOM from the other ($V_{\text{proj}} = 22 \text{ m/s}$).

We plot in Figure 26 the evolution of the maximum circumferential stress, i.e., along the direction θ_0 in the $(v_c, T\text{-stress})$ -space. One observes that the maximum value of $\sigma_{\theta\theta}^0$ does not necessarily account for crack branching as one would expect (the maximum value of $\sigma_{\theta\theta}^0$ is reached prior to the branching moment, i.e., before the arrowhead). In fact, as long as the crack propagation direction is $\theta_0 = 0$, the maximum stress (whatever its value) is along the extension of the crack, stabilising thus the propagation. However, if the crack direction diverges from the

Figure 26 Maximum circumferential stress map of the PMMA samples constructed from experimental measurements and fitted to Kanninen and Popelar (1985)'s empirical law. The history of the crack propagation in each sample is displayed, from the initiation at the notch (disc marker) until the branching position (triangle marker) ± 1 frame.



direction of the extension of the crack, instabilities and eventual branching occur. The deviation from $\theta_0 = 0$ is hence a sufficient condition to foster the instabilities, while the stress value is a necessary condition.

6 Concluding remarks

The unquestionable influence of the stress-waves on the crack propagation and their interactions with a moving crack-tip in a homogeneous material are highlighted. The analysis is lead in the SIF (dynamic fracture mechanics) concepts.

We build on the work of Ramulu and Kobayashi (1983) to mount a comprehensive (in)stability criterion that enables the assessment of the unquestionable role played by T -stress on crack branching and instabilities at relatively low crack-tip speeds. Indeed, this criterion predicted crack instabilities at lower crack-tip speeds than the ones elaborated in the classical dynamic fracture theory.

Moreover, the proposed formulation overcomes the limitations suffered by the criterion in Ramulu and Kobayashi (1983), namely, (1) the false prediction of crack instability at negative T -stress under near quasi-static loading (2) and the limitation related to the assessment crack speeds in the range $v_c < 0.67c_s = 0.72c_R$, making our proposition a comprehensive criterion for crack (in)stability assessment.

A validation of the analysis scheme is lead on crack-branching phase-field simulations and on a novel experimental setup.

We combine UHS-HR imaging technologies with cutting edge DIC algorithms on a novel experimental inertial impact test. A distinctive geometry that would yield interesting crack propagation and branching phenomena is considered. This configuration allowed the measurement of never-seen-before 400 kfps full-field kinematics. The most compelling captured phenomena are the compressive stress-waves entering the specimen, the cracks initiation and propagation, and of course crack branching as tensile stress-waves lengthwise of the crack meet its tip.

DIC measurements allow the extraction of relevant information regarding the fracture process, knowingly SIF, T -stress and the crack-tip speeds. From here, we showcase the role played by T -stress on the crack branching phenomena by analysing the direction of maximum circumferential stress at a reference distance r_c from the crack-tip along the propagation. Indeed instabilities are fostered as a co-action between the rapid propagating crack and the presence of a stress lengthwise of the crack direction T -stress. The most compelling findings regarding the dynamic (in)stabilities are summarised as follows.

1. T -stress plays a major role in dynamic (in)stabilities and limiting crack velocities. This role is put forth theoretically, numerically (phase-field simulations) and experimentally (highly resolved ultra-high-speed imaging + DIC). Understanding the role of T -stress in dynamic crack propagation is of great interest as the stress-state biaxiality at the crack-tip is inevitably continuously modified due to the stress-wave reflected from the boundaries and those emitted by the crack-tip interacting with the crack-tip itself. This is the case for example in architected material (Glacet et al. 2018; Eid et al. 2021; Somera et al. 2022), usually used as shock absorber, where the multiplication of

free edges makes the ‘ T -stress loading condition’ of a propagating crack varying all the time. The current work would provide crucial information for the design of such structures with respect to crack propagation.

2. The (in)stability map constitutes a straightforward visual tool for assessing dynamic (in)stabilities based on simple fracture mechanics concepts. The modification of the angular distribution of the stresses at a distance from the crack-tip due to its speed and the presence of T -stress are at its core.
3. We validate the capability of the proposed method to predict branching in phase-field simulation on a crack branching benchmark in which no loading along the crack propagation exist, and hence intuitively no T -stress should appear. Surprisingly, the observed branching develops as a positive T -stress appears at the crack-tip.
4. In phase-field simulations, damage bands are observed to widen. From the instability map, we see how the widening coincides well with a deviation into the transition zone (between stable and unstable crack propagation).

Although the proposed numerical and experimental tests seem to showcase the robustness of the advanced criterion, we believe that further investigation on test cases where cracks propagate and branch within larger ranges of tip speeds are needed. By that means, a more accurate fitting of the crack propagation law (Kanninen and Popelar 1985) can be enabled, from one side, and a more accurate r_c can be determined, from the other, making the criterion analysis incontestable.

6.1 On the potential of such criterion for crack branching

From DIC algorithms, coupled with UHS-HR imaging, one can propose a sound strategy that allows a more rigorous identification of the phase-field parameters based on a coupling between the crack tip speed, extractions of SIF and higher-order terms, inspired from (Réthoré and Estevez 2013).

Even though the phase-field modelling is a robust approach that requires no artificial criteria for crack initiation, crack coalescence or crack branching, the computation of the so-called damage field is usually made over the whole domain which naturally makes simulations computationally heavy especially since the mesh size is required to be at least smaller than 0.5 the internal length of the model leading to meshes with a large number of elements. From the material (in)stability a simple criterion for crack branching naturally emerges. We expect computationally efficient methods like X-FEM (Moës et al. 1999) to be enriched with such an effective criterion to judge crack branching. Instead of the more costly methodologies, knowingly the ones based on enriching the classical displacement field to model a multiple branched crack (via ‘junction’ functions (Daux et al. 2000) to relate two or more cracks), or the ones based on the loss of hyperbolicity in damage models (Belytschko et al. 2003), we believe that the herein proposed criterion can be a lighter alternative to study the branched crack using X-FEM. Evaluating T -stress via an interaction integral method for example (Paulino and Kim 2004), or the projection method used herein (Roux and Hild 2006; Roux et al. 2009) is a relatively straightforward task, and by carefully incorporating the critical distance r_c , the (in)stability map enables an effortless analysis of the (in)stabilities and crack branching.

6.2 On the reference distance r_c

Can r_c be linked to the notion of a process zone? We believe that r_c , as a critical distance that embodies a non-locality in the problem which allows the explanation of phenomena near the crack tip that could not be explained via the theory of dynamic fracture otherwise, is a philosophically sound concept to be related to the notion of a process zone. In statics, Döll (1983) measured a process zone in the PMMA of size 30 – 40 μm by Optical interference measurements. More recently, Réthoré and Estevez (2013) found a process zone size of the same order of magnitude (20 μm) by identifying a cohesive model using microscopic DIC displacement fields in the vicinity of the process zone (in the region where the K -fields are dominant). In dynamics, Bjerke and Lambros (2003) via a thermally dissipative cohesive zone model found a cohesive zone length up to 1206 μm = 1.2 mm. We believe that linking these quantities is an interesting avenue to be explored and more research has to be done around this subject.

A DIC fields and SIF results

A.1 TAF₂ Sample

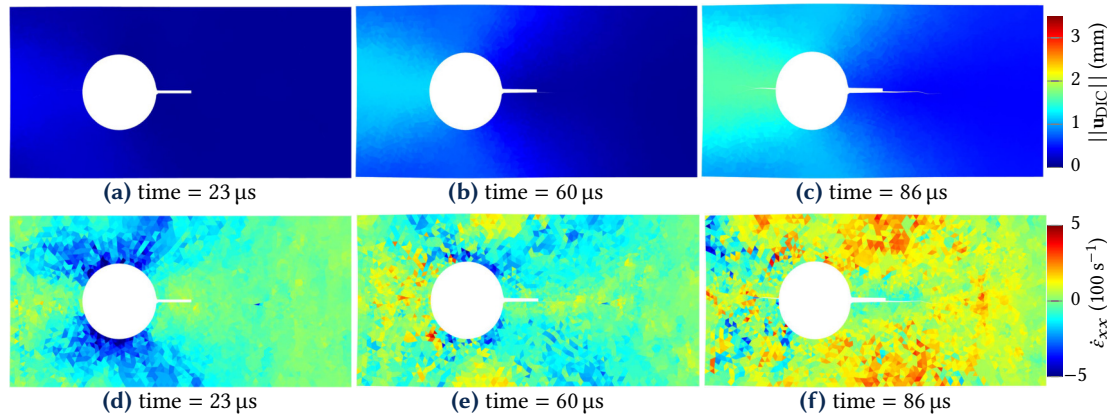


Figure A.1 Sample TAF₂-DIC displacement fields (top) and longitudinal strain rates (bottom) at three time steps. A Savitzky Golay (kernel size= 5 frames, order 2) filter smoothens the velocity fields. Spatial noise is filtered-out via a Tikhonov regularisation of the DIC problem.

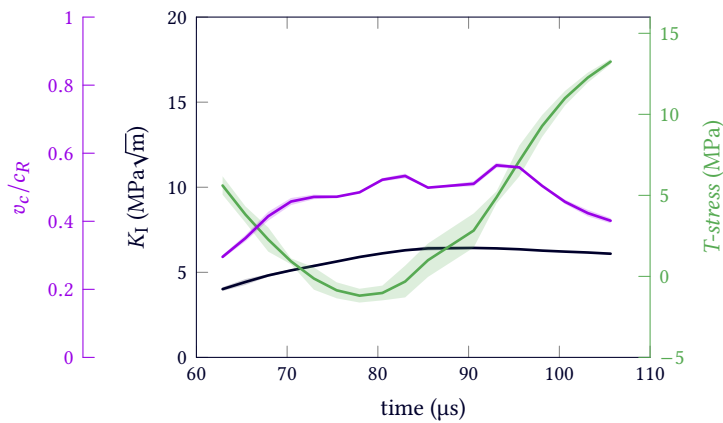


Figure A.2 Sample TAF₂-SIF higher-order term T -stress and crack tip speed. The error-bar corresponds to the sensibility to the extraction zone (Roux and Hild 2006; Roux et al. 2009).

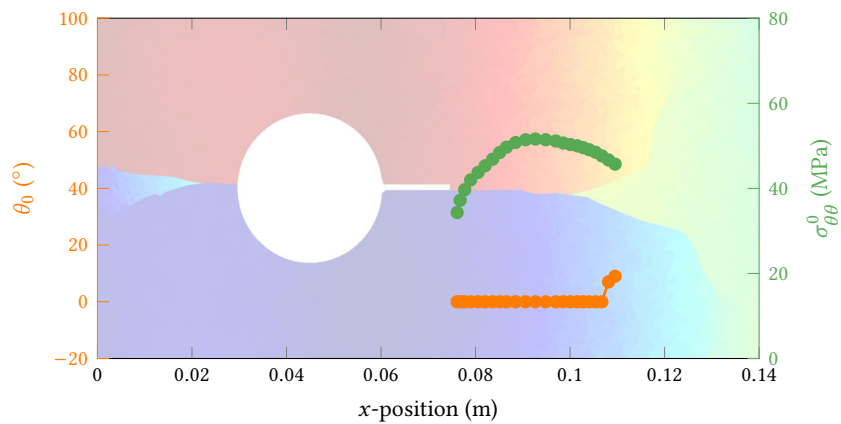


Figure A.3 Sample TAF₂-Predicted fracture direction θ_0 along with the maximum circumferential stress computed at $r_c = 2 \text{ mm}$. The modification of the fracture angle at the position of branching and the evolution of $\sigma_{\theta\theta}^0$ mirror the branching.

A.2 T₃DE Sample

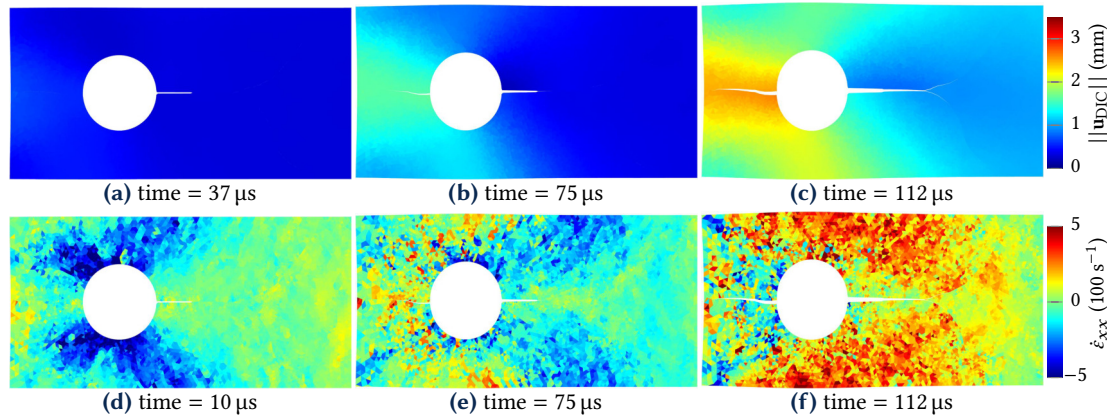


Figure A.4 Sample T₃DE–DIC displacement fields (up) and longitudinal strain rates (down) at three time steps. A Savitzky Golay (kernel size= 5 frames, order 2) filter smoothens the displacements’ first derivative (velocity fields). Spatial noise is filtered-out via a Tikhonov regularisation of the DIC problem.

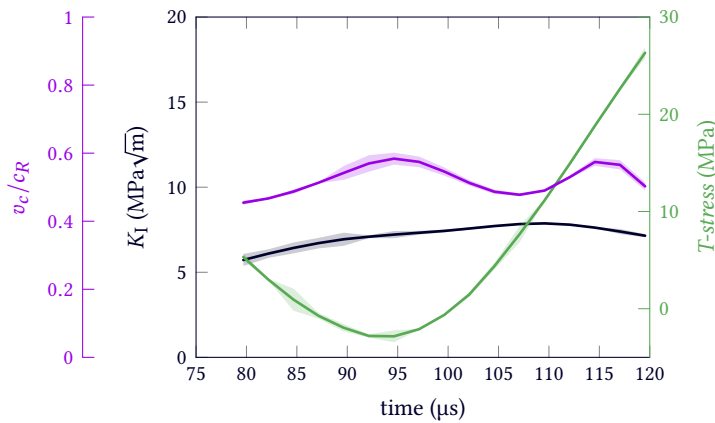


Figure A.5 Sample T₃DE–SIF higher-order term T -stress and the crack tip speed. The error-bar corresponds to the sensibility to the extraction zone (Roux and Hild 2006; Roux et al. 2009).

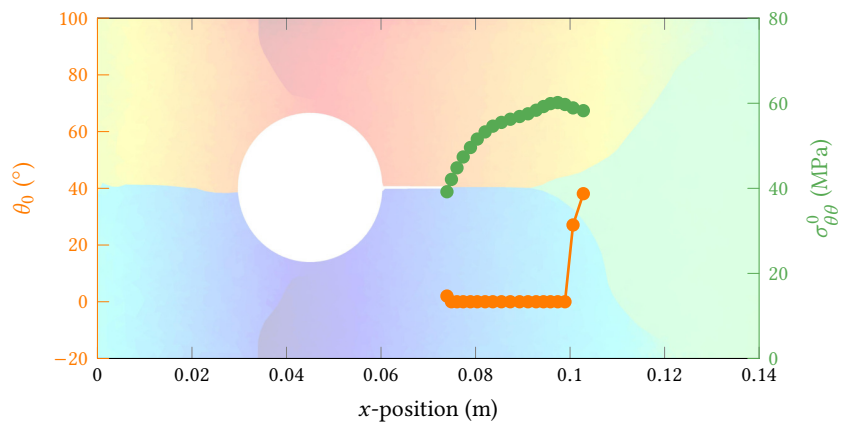


Figure A.6 Sample T₃DE–Predicted fracture direction θ_0 along with the maximum circumferential stress computed at $r_c = 2$ mm. The modification of the fracture angle at the position of branching and the evolution of $\sigma_{\theta\theta}^0$ mirror the branching.

A.3 THOM Sample

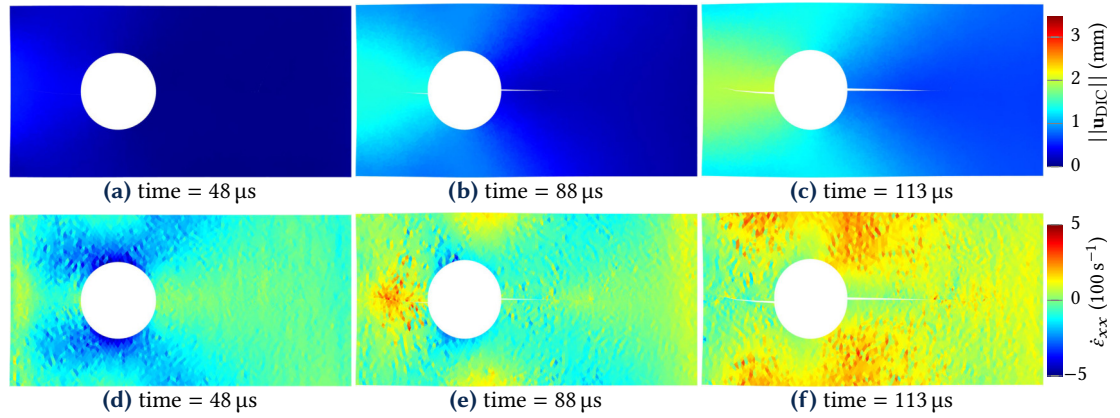


Figure A.7 Sample THOM–DIC displacement fields (up) and longitudinal strain rates (down) at three time steps. A Savitzky Golay (kernel size= 5 frames, order 2) filter smoothens the velocity fields. Spatial noise is filtered-out via a Tikhonov regularisation of the DIC problem.

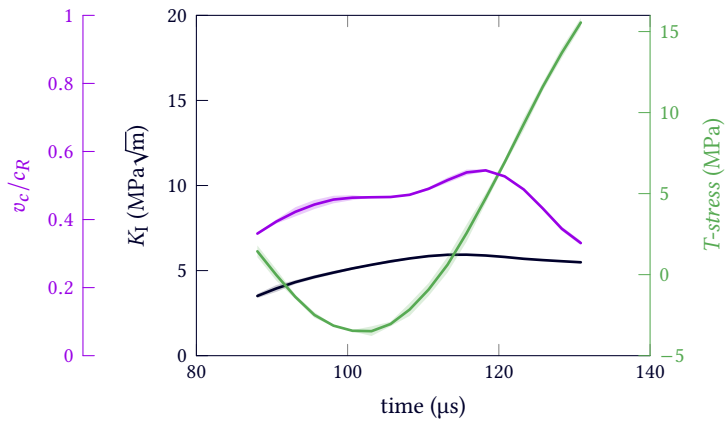


Figure A.8 Sample THOM–SIF: higher-order term T -stress and crack tip speed. The error-bar corresponds to the sensibility to the extraction zone (Roux and Hild 2006; Roux et al. 2009).

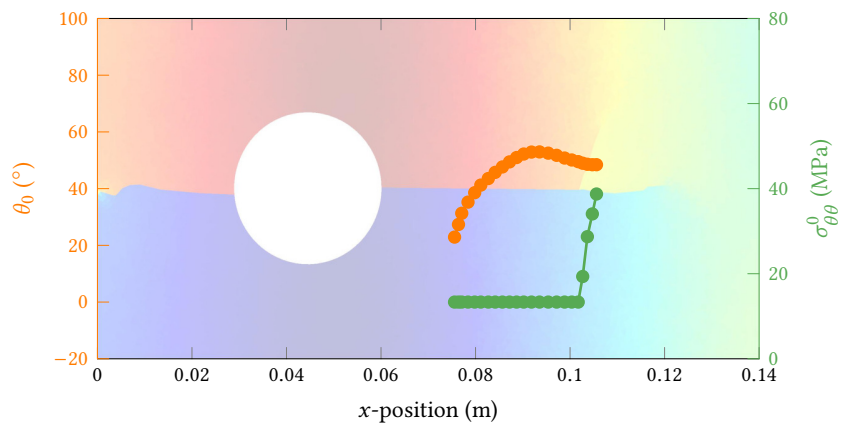


Figure A.9 Sample THOM–Predicted fracture direction θ_0 along with the maximum circumferential stress computed at $r_c = 2$ mm. Modification of the fracture angle at the position of branching and evolution of $\sigma_{\theta\theta}^0$ mirror the branching.

B Automatic SIF and crack-tip detection

B.1 SIF Extraction procedure

The extraction advanced in (Roux and Hild 2006; Roux et al. 2009) proceeds as follows.

1. A crack path is proposed—in the numerical simulations the crack path is easily tracked thanks to the damage variable α . During actual experiments, the crack path is obtained from images of the deformed sample transformed back to the Lagrangian configuration, see e.g. (Vinel et al. 2021).
 2. The size of the pacman-shaped extraction domain is defined by a circular area of radius r_{ext} from which a small band of width r_{int} is removed around the crack tip, see Figure B.10.
 3. The choice of the loading conditions (plane strain/plane stress) through κ is made.
- It is noted that κ can be added as a degree of freedom of the problem further validating the choice on the plane strain/plane stress conditions.

Throughout the extraction, the elastic crack tip position is updated using the first super-singular term $n = -1$, and the instantaneous SIF and T -stress are detected. The crack tip velocity v_c can be calculated consequently.

B.2 SIF Theoretical aspect

The SIF and T -stress measurement is essential for validating the role of non-singular terms on crack branching at low crack tip speeds. In this section, the considered methodology for the simultaneous detection of the crack path, the crack tip, the SIF and higher-order terms from displacement fields is put forth. The extraction scheme in (Roux and Hild 2006; Roux et al. 2009) is considered; it overcomes the inevitable sensitivity to noise found in previous methods; it can be indeed applied for extractions on curved cracks, and most prominently, is robust enough to be considered for analysing experimental displacement fields obtained via DIC on Ultra-High-Speed-High-Resolution images.

For a semi-infinite straight crack in a 2D elastic body subjected to a mechanical load, Williams (1957) proposed analytical solutions for:

- symmetric fracture modes (mode I):

$$\Phi_{\text{I}}^n(r, \theta) = r^{n/2} \left(\kappa e^{in\theta/2} - \frac{n}{2} e^{i(4-n)\theta/2} + \left(\frac{n}{2} + (-1)^n \right) e^{-in\theta/2} \right) \quad (\text{B.1})$$

- antisymmetric fracture modes (mode II):

$$\Phi_{\text{II}}^n(r, \theta) = ir^{n/2} \left(\kappa e^{in\theta/2} + \frac{n}{2} e^{i(4-n)\theta/2} - \left(\frac{n}{2} - (-1)^n \right) e^{-in\theta/2} \right) \quad (\text{B.2})$$

where the elementary solutions are indexed by n , and i is the pure imaginary number $\sqrt{-1}$. The displacement field for a stationary crack around its tip can be written as

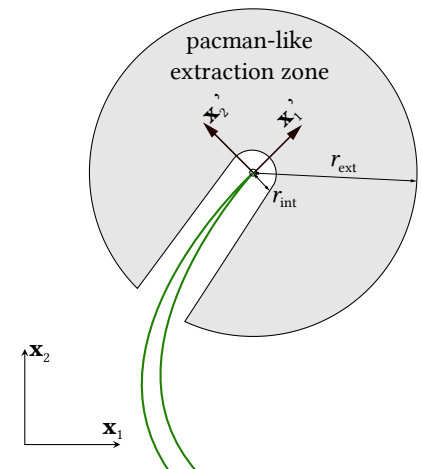
$$u(r, \theta) = \sum_{k=\text{I,II}} \sum_{n=-\infty}^{\infty} a_k^n \bar{\Phi}_k^n(r, \theta) \quad (\text{B.3})$$

where r and θ are the polar coordinates in the local frame of the crack tip (x'_1, x'_2) ; κ is Kolossov's constant; $\bar{\Phi}_k^n$ are the projection of Φ_k^n onto the $(\mathbf{x}_1, \mathbf{x}_2)$ coordinate system, a_k^n represent different coefficients in the solution, i.e., for $n = 1$, a_{I}^1 relates to K_{I} , and a_{II}^1 relates to K_{II} . Following (Roux and Hild 2006; Roux et al. 2009), the displacement fields \mathbf{u} —whether experimentally or numerically obtained—, are projected onto what is known as a truncation of the Williams' series (Williams 1957). The solutions that are used for projecting the displacement in a least-squares sense fields and extracting the fracture parameters are truncated between $n = n_m = -3$ and $n = n_M = 7$ lowering the degrees of freedom of the inverse problem while maintaining a family of solutions that contains sufficient information about the crack features:

- $n = 0$: rigid body translation,
- $n = 1$: asymptotic terms (K_{I} , K_{II}), and
- $n = 2$: T -stress and rigid body rotations.

In practice, especially in the experimental case, potential non-linear behaviour (plasticity, damage) close to the crack tip takes place. Since the methodology is based on an elastic description of the solid, only the mechanical behaviour outside a confined zone near the crack tip, see Figure B.10, should thus be studied. This bridging of the far-field elastic loading to the local crack tip happens without any issues regarding probable non-linear behaviour near the crack tip.

Figure B.10 Pacman-shaped extraction domain.




References

- Ambati, M., T. Gerasimov, and L. De Lorenzis (2015). A review on phase-field models of brittle fracture and a new fast hybrid formulation. *Computational Mechanics* 55(2):383–405. [DOI].
- Belytschko, T., H. Chen, J. Xu, and G. Zi (2003). Dynamic crack propagation based on loss of hyperbolicity and a new discontinuous enrichment. *International Journal for Numerical Methods in Engineering* 58(12):1873–1905. [DOI].
- Bjerke, T. and J. Lambros (2003). Theoretical development and experimental validation of a thermally dissipative cohesive zone model for dynamic fracture of amorphous polymers. *Journal of the Mechanics and Physics of Solids* 51(6):1147–1170. [DOI].
- Bleyer, J. and J.-F. Molinari (2017). Microbranching instability in phase-field modelling of dynamic brittle fracture. *Applied Physics Letters* 110(15):151903. [DOI], [HAL].
- Borden, M., C. Verhoosel, M. Scott, T. J. R. Hughes, and C. Landis (2012). A phase-field description of dynamic brittle fracture. *Computer Methods in Applied Mechanics and Engineering* 217-220:77–95. [DOI].
- Brugier, F. (2017). Modèle condensé de plasticité pour la fissuration et influence de la contrainte T . French. PhD thesis. France: Université Paris Saclay. [HAL].
- Brugier, F., Y. Guilhem, and S. Pommier (2015). Influence of T -stress on fatigue crack propagation. *6th International Conference on Fatigue Design* (Senlis, France, Nov. 18–19, 2015). [HAL].
- Cotterell, B. and J. R. Rice (1980). Slightly curved or kinked cracks. *International Journal of Fracture* 16(2):155–169. [DOI].
- Daux, C., N. Moës, J. Dolbow, N. Sukumar, and T. Belytschko (2000). Arbitrary branched and intersecting cracks with the extended finite element method. *International Journal for Numerical Methods in Engineering* 48(12):1741–1760. [DOI], [HAL].
- Döll, W. (1983). Optical interference measurements and fracture mechanics analysis of crack tip craze zones. *Crazing in Polymers*. Springer-Verlag, pp 105–168. [DOI].
- Eid, E., R. Seghir, and J. Réthoré (2021). Multiscale analysis of brittle failure in heterogeneous materials. *Journal of the Mechanics and Physics of Solids* 146:104204. [DOI], [OA].
- Erdogan, F. and G. C. Sih (1963). On the crack extension in plates under plane loading and transverse shear. *Journal of Basic Engineering* 85(4):519–525. [DOI].
- Finnie, I. and A. Saith (1973). A note on the angled crack problem and the directional stability of cracks. *International Journal of Fracture* 9(4):484–486. [DOI].
- Freund, L. B. (1998). *Dynamic Fracture Mechanics*. Cambridge University Press. [DOI].
- Glacet, A., J. Réthoré, A. Tanguy, and F. Morestin (2018). On the failure resistance of quasi-periodic

- lattices. *Scripta Materialia* 156:23–26. [DOI], [HAL].
- Grégoire, D., H. Maigre, J. Réthoré, and A. Combescure (2007). Dynamic crack propagation under mixed-mode loading – Comparison between experiments and X-FEM simulations. *International Journal of Solids and Structures* 44(20):6517–6534. [DOI], [OA].
- Gupta, M., R. C. Alderliesten, and R. Benedictus (2015). A review of T-stress and its effects in fracture mechanics. *Engineering Fracture Mechanics* 134:218–241. [DOI].
- Hussain, M. A., S. L. Pu, and J. Underwood (1974). Strain energy release rate for a crack under combined mode I and mode II. *National Symposium on Fracture Mechanics*. Ed. by G. Irwin. West Conshohocken: ASTM International, pp 1–27. [DOI], [HAL].
- Kanninen, M. and C. Popelar (1985). *Advanced Fracture Mechanics*. ISBN: 9780195035322.
- Kobayashi, A. S. and M. Ramulu (1985). A dynamic fracture analysis of crack curving and branching. *Le Journal de Physique Colloques* 46(C5):C5–197–C5–206. [DOI].
- Li, T., J.-J. Marigo, D. Guilbaud, and S. Potapov (2016). Numerical investigation of dynamic brittle fracture via gradient damage models. *Advanced Modeling and Simulation in Engineering Sciences* 3(1):26. [DOI], [OA].
- Liu, G., Q. Li, M. Msekh, and Z. Zuo (2016). Abaqus implementation of monolithic and staggered schemes for quasi-static and dynamic fracture phase-field model. *Computational Materials Science* 121:35–47. [DOI].
- Miehe, C., M. Hofacker, and F. Welschinger (2010). A phase field model for rate-independent crack propagation: Robust algorithmic implementation based on operator splits. *Computer Methods in Applied Mechanics and Engineering* 199(45–48):2765–2778. [DOI].
- Moës, N., J. Dolbow, and T. Belytschko (1999). A finite element method for crack growth without remeshing. *International Journal for Numerical Methods in Engineering* 46(1):131–150. [DOI], [HAL].
- Nguyen, T.-T., J. Yvonnet, D. Waldmann, and Q.-C. He (2020). Implementation of a new strain split to model unilateral contact within the phase field method. *International Journal for Numerical Methods in Engineering* 121(21):4717–4733. [DOI], [HAL].
- Palaniswamy, K. and W. G. Knauss (1978). On the problem of crack extension in brittle solids under general loading. *Mechanics Today*. Elsevier, pp 87–148. [DOI].
- Paulino, G. and J.-H. Kim (2004). A new approach to compute T-stress in functionally graded materials by means of the interaction integral method. *Engineering Fracture Mechanics* 71(13–14):1907–1950. [DOI].
- Pereira, L. F., J. Weerheijm, and L. J. Sluys (2017). A numerical study on crack branching in quasi-brittle materials with a new effective rate-dependent nonlocal damage model. *Engineering Fracture Mechanics* 182:689–707. [DOI].
- Pham, K. H., K. Ravi-Chandar, and C. M. Landis (2017). Experimental validation of a phase-field model for fracture. *International Journal of Fracture* 205(1):83–101. [DOI].
- Pierron, F., H. Zhu, and C. Siviour (2014). Beyond Hopkinson's bar. *Philosophical Transactions of the Royal Society A: Mathematical, Physical and Engineering Sciences* 372(2023):20130195. [DOI], [OA].
- Ramulu, M. and A. S. Kobayashi (1983). Dynamic crack curving—A photoelastic evaluation. *Experimental Mechanics* 23(1):1–9. [DOI].
- Ramulu, M. and A. S. Kobayashi (1985). Mechanics of crack curving and branching—A dynamic fracture analysis. *International Journal of Fracture* 27(3–4):187–201. [DOI].
- Ren, H. L., X. Y. Zhuang, C. Anitescu, and T. Rabczuk (2019). An explicit phase field method for brittle dynamic fracture. *Computers & Structures* 217:45–56. [DOI].
- Rice, J. R. and M. A. Johnson (1970). The role of large crack tip geometry changes in plane strain fracture. *Inelastic Behaviour of Solids*. Ed. by M. Kanninen. McGraw-Hill, pp 641–672. [OA].
- Ritchie, R. O., J. F. Knott, and J. R. Rice (1973). On the relationship between critical tensile stress and fracture toughness in mild steel. *Journal of the Mechanics and Physics of Solids* 21(6):395–410. [DOI], [OA].
- Roux, S., J. Réthoré, and F. Hild (2009). Digital image correlation and fracture: an advanced technique for estimating stress intensity factors of 2D and 3D cracks. *Journal of Physics D: Applied Physics* 42(21):214004. [DOI], [OA].
- Roux, S. and F. Hild (2006). Stress intensity factor measurements from digital image correlation:

- post-processing and integrated approaches. *International Journal of Fracture* 140(1-4):141–157. [DOI], [HAL].
- Réthoré, J. and R. Estevez (2013). Identification of a cohesive zone model from digital images at the micron-scale. *Journal of the Mechanics and Physics of Solids* 61(6):1407–1420. [DOI], [HAL].
- Réthoré, J., F. Hild, and S. Roux (2008). Extended digital image correlation with crack shape optimization. *International Journal for Numerical Methods in Engineering* 73(2):248–272. [DOI], [HAL].
- Schlüter, A., A. Willenbücher, C. Kuhn, and R. Müller (2014). Phase field approximation of dynamic brittle fracture. *Computational Mechanics* 54(5):1141–1161. [DOI].
- Sharon, E. and J. Fineberg (1996). Microbranching instability and the dynamic fracture of brittle materials. *Physical Review B* 54(10):7128–7139. [DOI].
- Somera, A., M. Poncet, N. Auffray, and J. Réthoré (2022). Quasi-Periodic Lattices: pattern matters too. *Scripta Materialia* 209:114378. [DOI], [OA].
- Streit, R. and I. Finnie (1980). An experimental investigation of crack-path directional stability: A photoelastic and experimental study on the effect of crack-tip stress biaxiality with respect to directional stability and fracture toughness of Mode I crack extension. *Experimental Mechanics* 20(1):17–23. [DOI].
- Van Blitterswyk, J., L. Fletcher, and F. Pierron (2018). Image-Based Inertial Impact Test for Composite Interlaminar Tensile Properties. *Journal of Dynamic Behavior of Materials* 4(4):543–572. [DOI], [OA].
- Vinel, A., R. Seghir, J. Berthe, G. Portemont, and J. Réthoré (2021). Metrological assessment of multi-sensor camera technology for spatially-resolved ultra-high-speed imaging of transient high strain-rate deformation processes. *Strain* 57(4). [DOI], [HAL].
- Williams, J. G. and P. D. Ewing (1972). Fracture under complex stress—the angled crack problem. *International Journal of Fracture Mechanics* 8(4):441–446. [DOI].
- Williams, M. L. (1957). On the stress distribution at the base of a stationary crack. *Journal of Applied Mechanics* 24(1):109–114. [DOI], [OA].
- Yoffe, E. (1951). LXXV. The moving Griffith crack. *The London, Edinburgh, and Dublin Philosophical Magazine and Journal of Science* 42(330):739–750. [DOI].

Open Access This article is licensed under a Creative Commons Attribution 4.0 International License, which permits use, sharing, adaptation, distribution and reproduction in any medium or format, as long as you give appropriate credit to the original author(s) and the source, provide a link to the Creative Commons license, and indicate if changes were made. The images or other third party material in this article are included in the article's Creative Commons license, unless indicated otherwise in a credit line to the material. If material is not included in the article's Creative Commons license and your intended use is not permitted by statutory regulation or exceeds the permitted use, you will need to obtain permission directly from the authors—the copyright holder. To view a copy of this license, visit creativecommons.org/licenses/by/4.0. 

Authors' contributions Elie EID and Julien RÉTHORÉ conceived the presented ideas. Elie EID developed the theory and performed the computations. Julien RÉTHORÉ and Rian SEGHIR verified and supervised the analytical methods. Rian SEGHIR and Julien RÉTHORÉ conceived and planned the experiments. Rian SEGHIR with support from Elie EID carried-out the experiments. All authors discussed the results and contributed to the final manuscript.

Supplementary Material Data for the four samples are available for download at the permalink [10.5281/zenodo.8256346](https://zenodo.org/doi/10.5281/zenodo.8256346). These include the raw images for each sample, along with the processed distortion-free images and all the corresponding data and information that are required to produce these findings.

Acknowledgements None.

Funding We acknowledge the financial support of Pays de La Loire, the city of Nantes and Ecole Centrale de Nantes through grant ConnectTalent IDS. The support of the French Research National Agency program through grant ANR-16-CE30-0007-01 is also acknowledged.

Ethics approval and consent to participate Not applicable.

Consent for publication Not applicable.

Competing interests The authors declare that they have no known competing financial interests or personal relationships that could have appeared to influence the work reported in this paper.

Journal's Note JTCAM remains neutral with regard to the content of the publication and institutional affiliations.